Stratigraphic reconstruction and analysis of the delta remnant Kodiak in Jezero Crater, Mars

Christian D Tate[1], Alexander G. Hayes[1], Oak Kanine[2], Sanjeev Gupta[3], Gwénaël Caravaca[4], Gerhard Paar[5], Stephane Le Mouelic[6], Christoph Traxler[7], and James Rice[8]

[1]Cornell University
[2]California Institute of Technology
[3]Imperial College
[4]UMR 5277 CNRS, UPS, CNES Institut de Recherche en Astrophysique et Planétologie
[5]JOANNEUM RESEARCH
[6]LPGN
[7]VRVis Zentrum für Virtual Reality und Visualisierung Forschungs-GmbH
[8]Arizona State University

April 16, 2024

Abstract

We analyze Kodiak, an eroded delta remnant in Jezero Crater, Mars, using several hundred images from the Mastcam-Z and SuperCam instruments on the Mars 2020 Perseverance Rover. We create a high-accuracy digital terrain model to measure Kodiak's stratigraphic layers, which we divide into three units and characterize individually. While each unit possesses geometries interpreted as consistent with a Gilbert-style delta formation, the older units exposed on Kodiak's north to northeast sides include more complex layered structures with azimuthally varying foresets. We compare Kodiak's northeast foresets with the clinoforms of Whale Mountain, an outcrop exposed in the Western Jezero Delta scarp, and show similar azimuthally varying foresets. The stratigraphic analysis presented herein (strike and dip, unit thickness, etc.) will help test and refine detailed sedimentological hypotheses for the formation and evolution of the Jezero delta. Our 3D reconstruction and measurements enable unprecedented precision to evaluate depositional models and advance geological interpretation.

Stratigraphic reconstruction and analysis of the delta remnant Kodiak in Jezero Crater, Mars

C. D. Tate[1], A. H. Hayes[1], O. A. Kanine[2], S. Gupta[3], G. Caravaca[4], G. Paar[5], S. Le Mouélic[6], C. Traxler[7], J.W. Rice, Jr.[8]

[1]Cornell University, Department of Astronomy and Planetary Science, Ithaca, NY, USA
[2]California Institute of Technology Division of Geological and Planetary Sciences, Pasadena, CA, USA
[3]Imperial College London, Department of Earth Science and Engineering, London, UK
[4]Institut de Recherche en Astrophysique et Planétologie, CNRS, Université de Toulouse, CNES, France
[5]Joanneum Research, Institute for Digital Technology, Graz, Austria
[6]CNRS Délégation Bretagne et Pays de Loire, Nantes, France
[7]VRVis Zentrum für Virtual Reality und Visualisierung Forschungs-GmbH, Wien, Austria
[8]Arizona State University, School of Earth and Space Exploration, Tempe, AZ, USA

Key Points:

- We present a digital 3D reconstruction of Kodiak sourced from over 400 images taken by the Mars 2020 Perseverance Rover.
- This science-grade model enables precise geometric measurements of Kodiak's strata that are essential for its geological interpretation.
- Kodiak's has at least three units, of which two have bedding layers with widely varying strikes that suggest fluvial processes.

Corresponding author: Christian Tate, cdt59@cornell.edu

Abstract

We analyze Kodiak, an eroded delta remnant in Jezero Crater, Mars, using several hundred images from the Mastcam-Z and SuperCam instruments on the Mars 2020 Perseverance Rover. We create a high-accuracy digital terrain model to measure Kodiak's stratigraphic layers, which we divide into three units and characterize individually. While each unit possesses geometries interpreted as consistent with a Gilbert-style delta formation, the older units exposed on Kodiak's north to northeast sides include more complex layered structures with azimuthally varying foresets. We compare Kodiak's northeast foresets with the clinoforms of Whale Mountain, an outcrop exposed in the Western Jezero Delta scarp, and show similar azimuthally varying foresets. The stratigraphic analysis presented herein (strike and dip, unit thickness, etc.) will help test and refine detailed sedimentological hypotheses for the formation and evolution of the Jezero delta. Our 3D reconstruction and measurements enable unprecedented precision to evaluate depositional models and advance geological interpretation.

Plain Language Summary

We examine an ancient delta remnant (named Kodiak) in Mars' Jezero Crater using images from the Perseverance Rover's Mastcam-Z and SuperCam. We created a detailed digital terrain model to analyze its layered structure, dividing it into several distinct units. Each unit showed features typical of a Gilbert-style delta, but the older layers on Kodiak's north and northeast sides were more complex. We compared these layers with similar formations. Our analysis includes detailed measurements of the layers' orientation and thickness and will refine our understanding of how the Jezero delta formed and evolved. This work required close collaboration among different teams operating the rover and its instruments. Despite camera calibration and image correlation challenges, our 3D models provide a precise view of Kodiak's geology, offering new insights into the Martian landscape.

1 Introduction

Kodiak is an 80 m tall and 250 m wide butte located less than a kilometer south of the Jezero Western fan scarp (Mangold et al. (2021)). The Western Jezero Delta, radiating from Neretva Vallis, was once likely connected to several hills or knobs scattered within a 10 km radius of the Neretva Vallis inlet before undergoing significant erosion (Schon et al. (2012); Goudge et al. (2015)). One such remnant, Kodiak, was continuously visible to the Perseverance rover throughout the first two years of the Mars 2020 mission and contains sedimentary strata that chronicle a portion of the depositional history of Jezero Crater and have been interpreted as indicators of an ancient lake environment (Mangold et al. (2021); Farley et al. (2022)). Kodiak's exposed bedforms (Fig. 1) were fortunately perpendicular to the rover traverse for this portion of the mission and, therefore, in a favorable alignment for rover-based imaging and long-baseline stereo reconstruction. Herein, we describe our new application of structure from motion (SfM) to over 400 images to generate a three-dimensional (3D) model of Kodiak's exposed stratigraphy. We use this Digital Terrain Model (DTM) to determine stratigraphic relationships in the Kodiak deposit and interpret the strike and dip of exposed beds in the context of a typical Gilbert-style delta.

Visualizing and characterizing geological features in three dimensions is crucial for their complete interpretation, and the lack of realistic and flexible rendering is a significant challenge for exploring remote, human-inaccessible locations like Mars. Recently, planetary geomorphologic studies have begun using Structure-from-Motion photogrammetry (SfM) to create 3D Digital Terrain Models (DTMs) of Martian terrains, such as the Kimberley outcrop (Caravaca et al. (2020)) and the Glen Torridon region (Caravaca et al. (2022)) in Gale Crater, that can be visualized in virtual reality (VR) environments for a more immersive and realistic experience of the terrain with its spatial relationships (e.g., Caravaca et al. (2020)). More traditionally, stereo photogrammetric processes are used to create DTMs on which researchers perform geometric analysis (e.g., Barnes et al. (2018); Banham et al. (2018, 2022); Traxler et al. (2022); Paar et al. (2023)) using software such as PRo3D (Traxler et al. (2022)) to obtain geometric measurements including strike and dip for each layer. While VR-compatible DTMs offer a rich visual context for qualitative geological interpretation (Barnes et al. (2018)), they cannot reach their full scientific potential without permitting quantitative analysis of layer thickness, dip angles, strike azimuths, and other geometric properties. Herein, we discuss a process that combines the immersive experience of the VR-compatible DTMs with the quantitative analysis of traditional DTMs to analyze Kodiak.

Early in its mission, the Mars 2020 Perseverance Rover documented Kodiak's East and North faces from various perspectives (Figs. 1 and 2). We use the data collected during this campaign to create a high-resolution DTM optimized bot for immersive VR environments and stratigraphic analysis tools such as PRo3D. We then use the model to measure the dimensions and orientations of various bedding packages observed in Kodiak's exposed stratigraphy. We build on the methodologies of prior studies (Caravaca et al. (2020); Barnes et al. (2018); Banham et al. (2018)) by combining the improved accuracy of multi-view SfM photogrammetry with a complete 3D analysis workflow to constrain Kodiak's stratigraphic relationships and interpret the strike and dip of exposed bedding layers in the context of a typical Gilbert-style delta. The DTMs, rendered orthographic mosaics, and plane measurements provided herein are used in other studies (Caravaca et al. and Kanine et al., both in this issue). These papers go beyond our present research and evaluate specific sedimentologic scenarios to explain our observations and measurements.

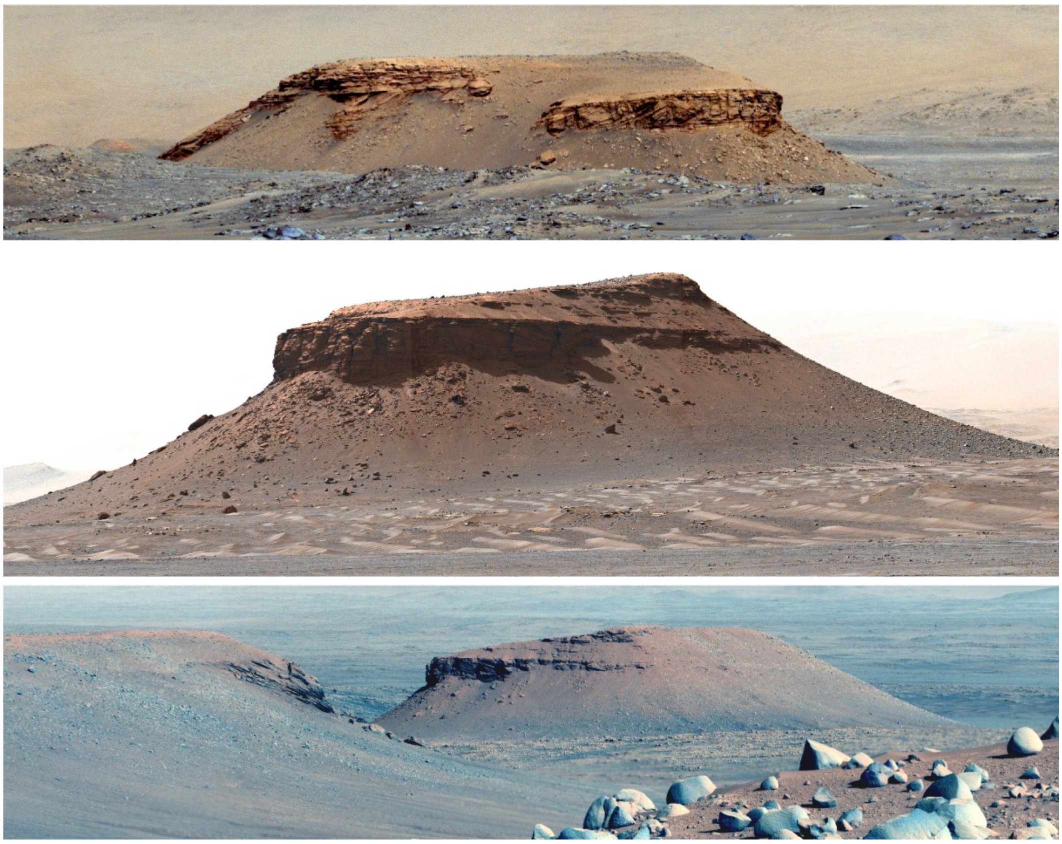

Figure 1. Mastcam-Z mosaics of Kodiak from several perspectives: (a) showing the eastern outcrops on Sol 83 (earth date), (b) northern outcrops on Sol 409 (April 14, 2022), and (c) the northwest side from Sol 753 (April 3, 2023) after climbing the delta and gaining 130 m of elevation. The structure on the left of (c) is the southern side of Whale Mountain. Image credits: NASA/JPL/MSSS/ASU.

2 Data

Our process uses radiance-calibrated (RAD) images taken from Sol 4 to Sol 580 (March 1, 2021 to Oct. 7, 2022) with two science instruments on the Mars 2020 Perseverance rover: the Mastcam-Z multispectral stereo imagers (Bell et al. (2021); Hayes et al. (2021); Kinch et al. (2020)) and SuperCam's Remote Micro-Imager (RMI) Maurice et al. (2021). The SuperCam RMI has a field of view (FOV) of about 1° with a pixel instantaneous field of view (IFOV) of 10µrad (Maurice et al. (2021); Wiens et al. (2021)). Although RMI images have more resolving power than the Mastcam-Z's, even at their highest zoom of 110 mm focal length (6° FOV and 67µrad IFOV, Hayes et al. (2021)), this comes at the expense of a restricted FOV. The best Mastcam-Z resolution on Kodiak is from a distance of 480 m, where its horizontal pixel scale is 3.3 cm. Kodiak's eastern outcrops were imaged from farther distances (1.9-3.2 km), with a best pixel scale of 13 cm.

This Kodiak imaging campaign required coordination between SuperCam, Mastcam-Z, and rover operations teams. As Perseverance progressed along its route and new perspectives of Kodiak came into view, the Mars 2020 science team requested observations to fill gaps in the butte's coverage. The imaging resolution of Kodiak varies across the campaign according to Perseverance's traverse; Table 1 summarizes Kodiak's Mastcam-

Z dataset and gives the estimated values for the resolution of each region of Kodiak captured. The reconstructed model shown in Fig. 3 uses over 400 Mastcam-Z images of Kodiak and its surrounding terrain along the rover traverse (shown in Fig. 2). Additional structural and textural detail comes from 52 SuperCam RMI images captured from six unique locations (Table S2).

The first 400 sols of the Mars 2020 mission included the Crater Floor Campaign (Horgan et al. (2023)), during which Perseverance imaged Kodiak's eastern face from azimuths between 65° to 102° and distances between 1.8 km and 2.6 km. Images from the Delta Front and Sample Depot campaigns Prepared by the Mars Sample Return Campaign Science Group (MCSG) et al. (2023) on sols 400-715 saw Kodiak's northern face from -36°N to 19°N azimuth and between 0.5 and 1.1 km distance and from an average of 32 m higher elevation than previous campaigns. The relative illumination and viewing geometries of Kodiak and the rover determined the most scientifically valuable time of day to take the images. The best images of eastern Kodiak in the first 400 sols were taken in morning lighting, while the best images of the often highly shadowed northern outcrops had evening illumination. We do not use images taken after Sol 700 because they have lower spatial resolution and do not significantly expand the coverage of Kodiak's most exposed outcrops.

Three dual-instrument sequences taken on Sols 63, 248, and 580 form the core of this dataset. Together, these images document about two-thirds of Kodiak. This region includes most of Kodiak's exposed outcrops above its wide scree and talus skirt judging from orbital views (Fig. 2).

3 Terrain Reconstruction

We use structure from motion (SfM) with the Mastcam-Z and SuperCam images (listed in supplementary Tables S1 and S2) to reconstruct the high-resolution digital terrain model (DTM) shown in Fig. 3. This model is viable and downloadable from Sketchfab from the following link: https://skfb.ly/oCyI8. We pre-processed each PDS image data product with a Python script that opened, transformed, and saved the images and camera model information in formats compatible with Agisoft Metashape. The localized exterior camera models are the primary metadata we extract from the PDS headers. These encode the image's position and orientation in a coordinate system compatible with the SfM software. This code used to perform this analysis is available on GitHub: https://github.com/cdt59/MPPP.

3.1 Long-baseline Stereo and Structure from Motion (SfM)

Long-baseline stereo techniques have precedence on Mars rover missions for capturing high-resolution topographic data (Caravaca et al. (2021)). These techniques typically involve capturing stereo pairs of images from two distinct but well-characterized positions, often separated by large distances relative to the target, to reconstruct the 3D geometry of the terrain. Such methods have been beneficial for navigational and scientific documentation, as they provide a quick way to obtain depth information from a scene (Maki et al. (2020); Bell et al. (2021)). However, traditional long-baseline stereo techniques often rely on single-pair stereo matching, which can be susceptible to calibration, alignment, and localization errors (Hayes et al. (2011); Barnes et al. (2018)).

In contrast, our approach employs Structure from Motion (SfM) as implemented in Agisoft Metashape Professional, which offers several advantages (Agisoft (2019); Le Mouélic et al. (2020); Over et al. (2021); Caravaca et al. (2021); Bistacchi et al. (2022); Paar et al. (2023)) as well as industrial applications (Paar et al. (2022)). SfM uses multiple images from different viewpoints to create a more self-consistent Digital Terrain Model (DTM). This method minimizes errors globally across the dataset by comparing tie points in one image to every other overlapping images, solving for each image's highest confidence depth map (Agisoft (2019); Over et al. (2021); Caravaca et al. (2021)). The resulting 3D model is more accurate and comprehensive because it minimizes camera model errors over all images and control points. Thus, while long-baseline stereo provides a robust but sometimes limited snapshot of the Martian terrain, our SfM approach creates a more detailed and accurate 3D reconstruction.

3.2 Rover Localization

Perseverance operations align each end-of-drive location with a Mars 2020 basemap and make these rover waypoints available for science analysis. The Mars 2020 basemap is made from a mosaic of orbital HiRISE images and has a resolution of about 25 cm (Stack et al. (2020); Farley et al. (2020)). Accurate rover and camera localization are required to generate precise models at their location, orientation, and scale. The estimated position and orientation of the image are made in Site Frame as obtained from the JPL localization process (Calef et al. (2023); Crumpler et al. (2023); Ruoff, N. A., Deen, R. G., Pariser, O. (2023)) to ensure that the SfM algorithm has the best available initial camera models for correctly triangulating points in space, thereby generating a reliable and high-fidelity 3D model. Inaccurate localization data can introduce errors in the reconstructed geometry, leading to distortions or misalignments in the resulting DTM. Moreover, precise localization allows for effectively merging data from different imaging campaigns or instruments, such as Mastcam-Z and SuperCam's Remote Micro-Imager, into a single, coherent model. This is particularly crucial when the model aims to capture complex geological features like the strata exposed at Kodiak.

3.3 Reconstruction Error

Two sources of error dominate the accuracy and precision of 3D reconstructions: uncertainties in the geometric camera model and range errors originating from correlation uncertainties. Although the Mars 2020 cameras are robustly calibrated in the rover coordinate system (Maki et al. (2020); Hayes et al. (2021)), the absolute camera positions are less constrained in the Mars-fixed coordinate system in which the vehicle estimates its position and orientation as it drives through the terrain. This introduces projection errors that structure from motion mitigates by optimizing camera parameters in a global control network. These projective errors are distinct from a second source: range error, the precision with which a stereo pair of images can correlate features and estimate their position in space with triangulation. Range error is in the line-of-site or range direction and increases quadratically for a fixed stereo base length. Because range error only quantifies the sub-pixel correlation between two stereo images, it is not a valid estimate of a model's overall reconstruction quality. Nevertheless, we assume that range errors are the primary source of non-correlated errors. As such, range error limits the relative position of points on the model surface for plane-fitting strike and dip analysis.

The theoretical range error is a standard but limited measure of reconstruction error. Similar to how imaging resolution estimates the precision of the image projection onto the model, the range error estimates the precision in the third axis (i.e., the range axis, which is orthogonal to the image's line and sample axes). Each well-characterized stereo pair can yield a digital terrain model (DTM) with a pixel-by-pixel accuracy determined by the camera properties and the relative geometry of imaging locations and the terrain. We estimate range errors for this model are comparable to the pixel scale, which is 3.3 and 13 cm for Kodiak's north and east faces, respectively (Table 1). Further details about our methodology for estimating the 3D reconstruction error are in S2 of the online supplementary materials.

Table 1. Summary of the Mastcam-Z observations of Kodiak, which we separate into four azimuth ranges relative to Kodiak. These are limited to Mastcam-Z sequences taken at its highest resolution zoom level at 110mm.

	East	**Northeast**	**North**	**Northwest**
sol range	004 – 275	382 – 388	409 – 711	750 – 756
imaging locations[1], total	23	3	11	3
imaging locations[1], used[2]	8	3	6	0
SuperCam locations[3], total	3	0	3	0
preferred time of day [4]	morning	morning	afternoon	evening
local mean solar time	7:58 – 11:38	8:10 – 9:36	10:04 – 16:00	11:46 – 16:03
local mean solar time, average	10:20	9:10	13:20	14:30
range[5] [km]	1.8 – 2.4	2.5 – 3.2	0.48 – 1.1	2.4 – 2.5
range[5], average [km]	2.2	2.8	0.71	2.5
elevation [m]	-5.3 – 1.8	-1.3 – 2.2	21 – 48	127 – 133
elevation, average [m]	0.0	0.3	32	130
azimuth[6] [°North]	84° – 102°	64° – 79°	324° – +19°	315° – 320°
azimuth[6], average [°North]	92°	73°	348°	318°
pixel scale, average [cm/pixel]	15	19	4.8	17
pixel scale, best [cm/pixel]	12	17	3.2	16
range error[7], average [cm]	140	98	4.4	160
range error[7], best [cm]	35	24	2.2	55

[1] See Table S1 or the online spreadsheet for details on each Mastcam-Z sequence.

[2] The values below are only for used sequences. See Table S1.

[3] This is the total number of SuperCam RMI sequences taken in each region. See Table S2 for details. All other information in this table is for the Mastcam-Z sequences.

[4] The Sun's incidence angle is important for capturing the fine details on Kodiak because of its many vertical outcrops. The preferred time of day is when the outcrop is best illuminated, which happens when the Sun is approximately behind the camera.

[5] We calculate range as the distance from the rover's location to a reference point in Kodiak (the center of curvature of Unit 1, which we assume to be 2335 m West, 244 m South, and 50 m above the O.E.B. landing site). See the downloadable supplementary spreadsheet for each imaging location's relative Northing, Easting, and Elevation.

[6] We calculate azimuth as the clockwise angle from North to a reference point in Kodiak (the center of curvature of Unit 1).

[7] See section S2 for how we calculate range error and recommend interpreting it.

3.4 Geometric measurements

We inspect and annotate the model using the Planetary Robotics 3D Viewer software abbreviated PRo3D (Barnes et al. (2018); Traxler et al. (2022)). The PRo3D software imports DTMs and provides several annotation tools that we use to trace the outcrop layers and measure their strike and dip angles. PRo3D uses the plane-fitting algorithm to calculate layer orientation and error. This algorithm uses principal component analysis (PCA) described in (Quinn & Ehlmann (2019)) to constrain layer geometry and estimate measurement uncertainty. Additional information about PRo3D and annotation files used for our measurements can be found in S3 and S4. The XYZ points extracted from our layer tracings are available in the supplementary materials for future researchers who want to use alternative methods for determining layer orientation.

4 Results

We divide the stratigraphy of Kodiak butte into three units, each containing inclined beds bounded by sub-horizontal beds and separated by truncation surfaces. We adopt the naming convention used in Caravaca et al. (this issue) and describe Units 0, 1, and 2 in stratigraphic order, as shown in Fig. 3. Table 2 lists each unit's average sequence thickness, dip, and strick measurements.

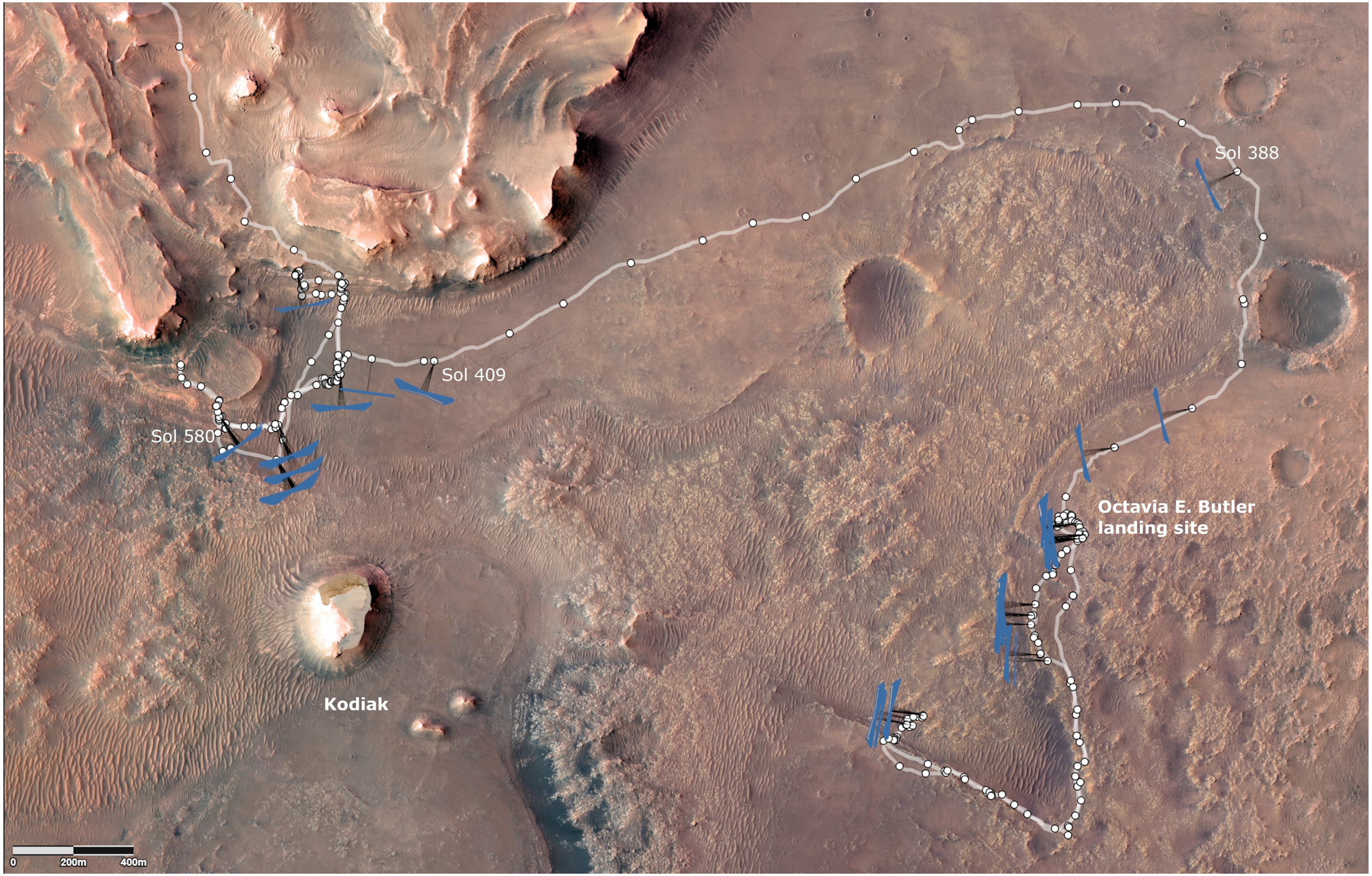

Figure 2. The Mars 2020 basemap of the Jezero Crater (primarily made from HiRISE mosaics) and the traverse of the Perseverance rover for the first 715 Sols of the Mars 2020 mission. The white dots show the locations where the rover stopped to take images, and the blue and black symbols show the positions and pointing of the Mastcam-Z images used to reconstruct Kodiak.

4.1 Unit 0

Unit 0 outcrops on the northwest flank of Kodiak butte. Scree covers its lower layers, making it the only unit without visible bottomsets. Unit 0 consists dominantly of variably inclined strata that extend laterally for about 60 m, as measured from our SfM model. It shows average and maximum thicknesses of 2.5 and 3.7 m, respectively. A convex-up sedimentary body in the center of Unit 0 is 6 m wide and 1 m high and has inclined layers on both flanks. Overlying this convex-up feature, we measure a range of dips between 15 to 25°, predominantly towards the northeast, at 35°N. At the east side of the outcrop, Unit 0's foresets are truncated by onlapping inclined layers of Unit 1. On top of the inclined layers, a sub-horizontal erosion surface separates them from sub-horizontal topset beds. These topsets appear to be stratigraphically equivalent to Unit 1's topset.

4.2 Unit 1

Unit 1 outcrops Kodiak's northeast flank. The lower part consists of over 5 m of sub-horizontal strata that dip $\sim 5°$ approximately to the south $\sim 179°$N. Another apparent outcrop of Unit 1's sub-horizontal strata occurs lower on the northeast corner of the butte. These layers appear to be in place, indicating about 10 m of sub-horizontally stratified rocks within the lower part of Unit 1.

The inclined beds of Unit 1 extend over 160 m from the middle of Kodiak's northern face to the middle of its eastern face. These layers have a range of dip azimuths between 180°N and $\sim 250°$N at Unit 1's southern and western extents, respectively. The inclined layers on the northwest side of Unit 1 onlap the inclined layers of Unit 0. At this interface between Units 1 and 0, the bedding dip azimuths are approximately opposite. Cobble-sized clasts (0.1-0.2 m in diameter) are embedded in Unit 1 close to this boundary, and these rounded grey clasts stand out against the nominal red appearance of Kodiak's strata. The inclined strata in the rest of Unit 1's northern exposure show a 6-7.2 m thick section of sigmoidal layers. Although the dip and strike geometries are complex to constrain on this flat outcrop face, they are consistent with dip azimuths to the southwest (Fig. 3).

Kodiak's strata at its northeast corner (or "nose") appear to be plunging into the outcrop. This is the boundary between Unit'1 north and east inclined layers, which we characterize as the point of greatest dip azimuth divergence. The outcrop at this crucial location is weathered, crumbly, and only obliquely imaged in shadow. Despite these difficulties, our reconstructed model reveals a doming pattern that is not apparent from the separate inspection of the original images. The inclined beds dip in divergent directions on both sides of this junction. Unit 1 North dips towards $\sim$ 230°N, and Unit 1 East dips towards 180°N. The latter contains the tallest and steepest inclined beds measured on Kodiak, at about 9 m tall and 40° dip towards the south. At the southern extent of Unit 1, the inclined beds shallow to dip angles of about 10°.

The upper sub-horizontal layers appear equivalent across both sides of Unit 1's east-north junction and with the topsets of Unit 0. However, on the southern end of Unit 1, the truncation surface appears to fade as the overlying strata drapes more continuously with the shallowly dipping inclined beds below.

4.3 Unit 2

Unit 2's lower sub-horizontal layers appear continuous with Unit 1's inclined beds, although scree covers large areas separating these two units. This package is up to 10 m thick, making it the thickest sub-horizontal part of Kodiak. This outcrops in the middle of Unit 2 and at its southern extent. The inclined beds of Unit 2 range between 2 to 5.6 m thick with an average of 4 m. Like Unit 1, the southernmost beds are shallow to about 10° dip. Unlike Unit 1, however, all the inclined strata dip towards a consistent azimuth of 135°N.

The sub-horizontal layers overlying Unit 1 are inclined at an average dip of 4.1° towards the same azimuth of 134°N. At the interface of the inclined strata and overlying sub-horizontal strata, scouring and crossbedding are observed. Unit 2 also outcrops on Kodiak's north side above Units 0 and 1. Here, the strata show cross-bedding similar to the equivalent layers on Kodiak's southern end. However, the orientation of these exposures to their probable dip directions is not favorable for reliable measurements of dip and strike.

4.4 Unit 3

Unit 3 is a deposit of boulders and cobbles overlying Unit 2's topsets. The most visible boulders have 0.5 m diameters, and we measure the largest as wide as 2 m. There does not appear to be any strata in Unit 3; hence, we do not include it in Table 2.

Table 2. Measurements on the 3D reconstruction of Kodiak. These give the horizontal scale of each major sequence, the number of strike and dip measurements on suitable outcrops, and their average values of dip angle and azimuth. After projecting each vector into the horizontal plane, we calculated the average azimuth values. Kodiak is divided into three units, as illustrated in Fig. 3, with Unit 1 further differentiated between east and north to highlight its variation in dip azimuth directions.

	Unit 0	**Unit 1, North**	**Unit 1, East**	**Unit 2**
Mastcam-Z resolution [cm]	3.3	3.3	18	13
outcrop exposure width [m]	60	80	100	120
topset height [m]	2.0	2.0	2.5	9.7
topset measurements	3	9	5	48
topset dip [°]	5.7	4.9	5.4	4.1
topset azimuth [°N]	342	347	232	134
foreset height [m]	2.5	5.9	7.7	4.0
foreset max height [m]	3.7	7.2	9.0	5.6
foreset measurements	11	29	40	21
foreset dip [°]	18.8	29.2	28.1	27.0
foreset azimuth [°N]	35	229	180	135
bottomset height [m]	-	>3	>2	10
bottomset measurements	-	1	9	3
bottomset dip [°]	-	∼8	4.5	∼6.6
bottomset azimuth [°N]	-	∼160	179	∼148

5 Discussion

Our 3D digital outcrop model of Kodiak butte provides an unprecedented opportunity to measure the quantitative geometry of its exposed layers. In Unit 2, Kodiak shows structures consistent with the previously proposed Gilbert delta model (Mangold et al. (2021)), with the central section comprising foreset beds that smoothly transition into bottomset strata at their base and overlying topset strata that abruptly terminate the foresets at their top. The foreset beds in Unit 2 show a consistent dip of 30° to the southeast, while the topsets and bottomsets dip about 3-8° in the same direction. These observations alone suggest a Gilbert-style delta depositional model for Kodiak with the delta lobe prograding basinward from the Neretva Valis inlet to the southeast at 140°N.

Within Units 0 and 1, however, the layers appear to have a more complex structure than the typical Gilbert-style deltaic succession shown in Unit 2. Not only does Unit 1's bedding azimuths change throughout the exposure, but these dip angles are also the

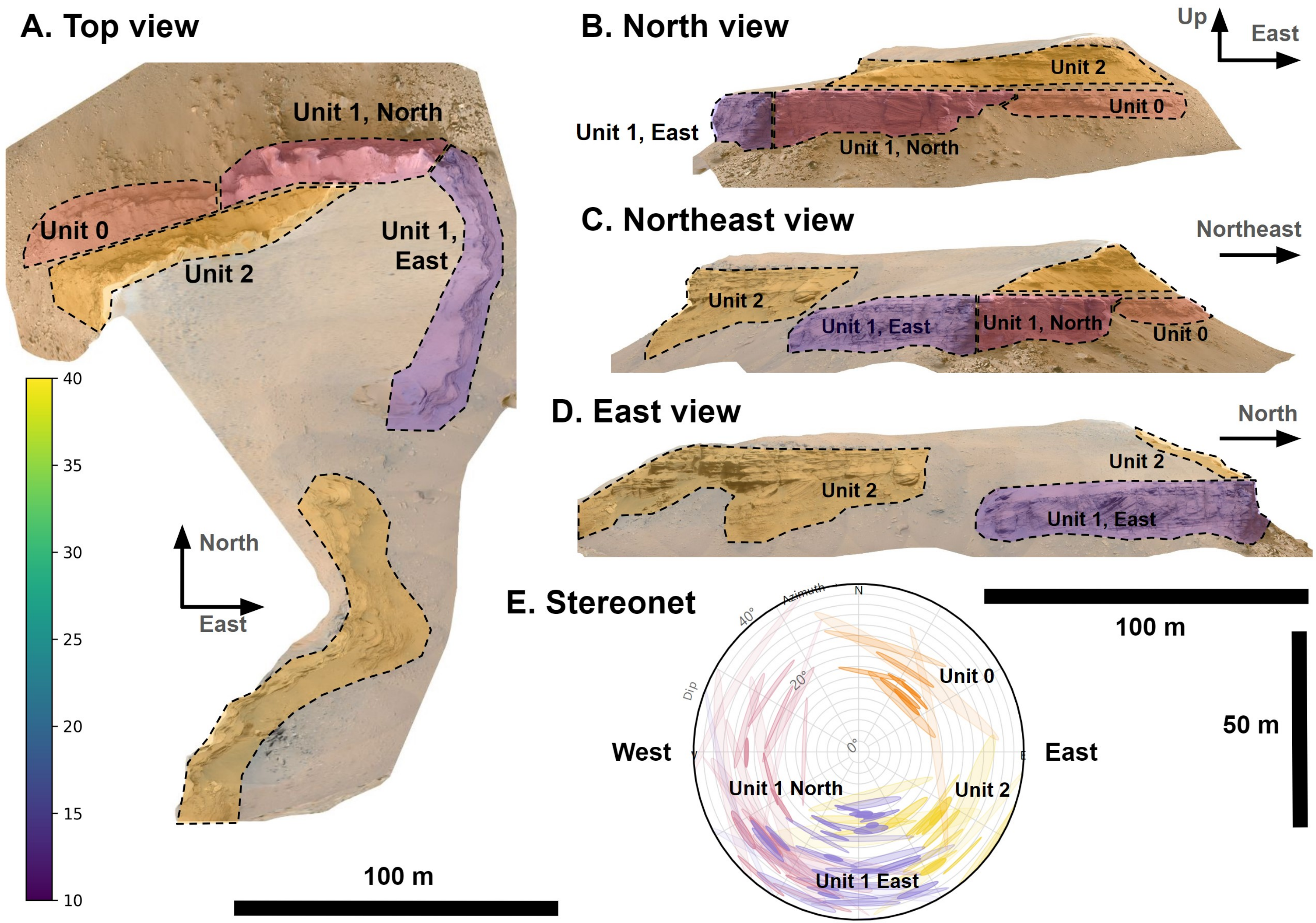

Figure 3. Rendered images of Kodiak's 3D reconstruction. Dashed lines show the approximate boundaries of Kodiaks' three stratigraphic units. (a) is a vertical orthographic projection of Kodiak with superimposed strike and dip symbols showing the dip magnitudes and azimuth orientations for each unit characterized in this study. The side views of Kodiak are orthographic projections (b) from the north, azimuth $0°N$, (c) from azimuth $45°N$, and from the east, azimuth $90°N$. (e) Stereonet of the foreset strike and dip measurements with their error ellipses Quinn & Ehlmann (2019).

steepest measured at Kodiak. Foreset strata in Units 0 and 1 indicate different accretion directions across a small lateral extent (∼50 meters), indicating deposition within narrow, overlapping delta lobes (Caravaca et al., this issue). The foresets of unit 1 also have the greatest thickness on Kodiak, with a 9.0 m maximum foreset thickness on its eastern face. As seen in Table 2, these vertical heights are considerably larger than Units 0 and 2. These measurements on Units 0 and 1 reveal geometrical complexity that may challenge a deltaic depositional hypothesis for Kodiak (see Kanine et al., this issue).

5.1 The narrow deltaic lobe interpretation

Unit 1 contains foreset beds that diverge ∼60° in azimuth over a horizontal distance of less than 50 m. This suggests that the original geometric planform of the foreset-containing sedimentary body was a relatively narrow lobate, convex-up form. Meanwhile, Unit 0 has irregular structures and an average dip direction of foreset beds opposite to Unit 1, indicating that it represents a different sedimentary body that accreted in an other direction. The northeast "nose" of Kodiak's Unit 1 could be a delta lobe that prograded to the southwest. Although its ∼50 m radius of curvature is narrow for a delta lobe, this scale is consistent with a relatively young lobe (Barrett et al. (2020)).

5.2 Comparisions to the main Western delta front

The leading Western delta front contains foreset structures similar to those observed at Kodiak. Whale Mountain (SF model), for instance, is the closest part of the Western Delta to Kodiak. Fig. S4 shows Whale Mountain's dip directions and how their radius of curvature has a similar ∼50 m scale as the diverging clinoforms we measured on the northeast side of Kodiak's Unit 1. While Kodiak's outcrop is neither well-preserved (highly weathered and degraded) nor well-imaged (in shadow and foreshortened by its off-normal orientation relative to the imaging direction), Whale Mountain presents a clean, vivid outcrop. Mastcam-Z imaged it on Sol 614 in optimal illumination and 1 cm/pixel (more than three times finer resolution than the best on Kodiak). Images from the delta top campaign imaged the western side of Whale Mountain (Sols 753, 756, 762), and show that its dip azimuths diverge a total of ∼180°. This is a more extreme dip azimuths divergence than the ∼50° measured on Kodiak. If there is a valid comparison between the narrow delta lobe interpretation of Kodiak Unit 1 and the similar structure of Whale Mountain, then studying the latter could be essential to understanding Kodiak.

Other structures on the delta front have foresets with vertical outcrops of over 20 m, which are far taller than Kodiak's maximum foreset height of 10 m. These locations on the delta front (in order of closest to farthest from Kodiak) are Mount Juhle (imaged on Sol 614, 625) (https://skfb.ly/ozZ9P), Franklin Cliff (Sol 696, 704) https://skfb.ly/oMpYF), and finally the Minors Castle and Morro Rock area (Sol 397, 398) on the easternmost extent of the Western Delta https://skfb.ly/oJp8U). Franklin Cliff is especially interesting for its preserved contact between foresets and topsets. These and other structures on Jezero's Western delta front are analyzed by Gupta et al. (this issue). Future studies should examine the deltaic environment required to produce horizontally curving foresets and how deltaic advancement could be toward the southwest, and compare these findings with evidence in the Western delta.

5.3 Comparisions to other delta rements

Two other remnants named Dragonera and Cabrerae stand southeast of Kodiak. Although smaller and more weathered than Kodiak, Cabrere contains outcrops southwest dipping foresets and bottomsets similar to those seen on Kodiak (albeit ∼50 meters lower elevation). Dragonera and the more distal remnants, such as Santa Cruz (images on Sols 36, 123) and Isle Royale (Sol 676) to the east and Pilot Pinnacle (Sol 128) to the south, are smoother and do not have analogous outcrops. It is unknown what causes this range of geomorphic expressions (Goudge et al. (2018); Quantin-Nataf et al. (2023)), but we find inclined beds resembling foresets only on the two remnants closest to the Western Delta.

6 Conclusion

We present a detailed 3D digital outcrop model of the Kodiak butte created from the fusion of hundreds of Perseverance Rover images. Stratigraphic analysis of the resulting DTM expands upon previous interpretations of Kodiak as deposits from a Gilbert-style delta with quantitative measurements. Our study shows the foreset strike azimuths change systematically over Kodiak's north and northeast outcrops. The depositional environments preserved in Kodiak are related to the enormous Western Delta fan, and investigating Kodiak can advance our understanding of Jezero's other deltaic structures throughout the crater floor.

7 Data Availability Statement

This study utilizes data from Mars rover imaging, which are archived and accessible through the Planetary Data System (PDS). The end data products derived from these images and our processing are included in the supplementary materials of this article for ease of reference and use. In adherence to the FAIR Data principles, we ensure that our data is Findable, Accessible, Interoperable, and Reusable. Descriptions and access instructions for all other utilized data and software tools, which are publicly available, and can be found in (Tate, 2023).

Acknowledgments

The Mars 2020 Mastcam-Z and SuperCam teams were tremendously influential in collecting and formatting these images. Another thanks to NASA's Planetary Data System (PDS), from which all the data used in this study are publicly available. The JPL Mars 2020 Localization Team provided the localization and pose for each Perseverance rover end-of-drive location. Joanneum Research and VRVis receive funding from the Austrian Research Promotion Agency, ASAP-18 Project 892662 "Mars-3D". VRVis is funded by BMK, BMAW, Styria, SFG, Tyrol, and Vienna Business Agency in the scope of COMET - Competence Centers for Excellent Technologies (879730), which FFG manages.

References

Agisoft, L. L. C. (2019). Agisoft metashape user manual: Professional edition. *Version*.

Banham, S. G., Gupta, S., Rubin, D. M., & others. (2022). Evidence for fluctuating wind in shaping an ancient martian dune field: The stimson formation at the greenheugh pediment, gale crater. *Journal of*.

Banham, S. G., Gupta, S., Rubin, D. M., Watkins, J. A., Sumner, D. Y., Edgett, K. S., … Vasavada, A. R. (2018, June). Ancient martian aeolian processes and palaeomorphology reconstructed from the stimson formation on the lower slope of aeolis mons, gale crater, mars. *Sedimentology*, *65*(4), 993–1042.

Barnes, R., Gupta, S., Traxler, C., Ortner, T., Bauer, A., Hesina, G., … Tao, Y. (2018, July). Geological analysis of martian rover-derived digital outcrop models using the 3-D visualization tool, planetary robotics 3-D viewer-PRo3D. *Earth Space Sci.*, *5*(7), 285–307.

Barrett, B. J., Gawthorpe, R. L., Collier, R. E. L., Hodgson, D. M., & Cullen, T. M. (2020, February). Syn-rift delta interfan successions: Archives of sedimentation and basin evolution. *Depositional Rec.*, *6*(1), 117–143.

Bell, J. F., 3rd, Maki, J. N., Mehall, G. L., Ravine, M. A., Caplinger, M. A., Bailey, Z. J., ... Wolff, M. J. (2021, February). The mars 2020 perseverance rover mast camera zoom (Mastcam-Z) multispectral, stereoscopic imaging investigation. *Space Sci. Rev.*, *217*(1), 1–40.

Bistacchi, A., Mittempergher, S., & Martinelli, M. (2022, April). *Digital outcrop model reconstruction and interpretation.* Wiley.

Calef, F. J., Parker, T. J., Schroeder, J., Williams, N., & Golombek, M. P. (2023, March). *Spatial products and services for the mars2020 perseverance rover* (Vol. 2806). ui.adsabs.harvard.edu.

Caravaca, G., Le Mouélic, S., Mangold, N., Jonas, L., Laetitia, L. D., & Marion, M. (2020, March). 3D digital outcrop model reconstruction of the kimberley outcrop (gale crater, mars) and its integration into virtual reality for simulated geological analysis. *Planet. Space Sci.*, *182*, 104808.

Caravaca, G., Le Mouélic, S., Rapin, W., Dromart, G., Gasnault, O., Fau, A., ... Lanza, N. L. (2021, October). Long-distance 3D reconstructions using photogrammetry with curiosity's ChemCam remote Micro-Imager in gale crater (mars). *Remote Sens. (Basel)*, *13*(20), 4068.

Caravaca, G., Mangold, N., Dehouck, E., Schieber, J., Zaugg, L., Bryk, A. B., ... Lanza, N. L. (2022, September). From lake to river: Documenting an environmental transition across the Jura/Knockfarril hill members boundary in the glen torridon region of gale crater (mars). *J Geophys Res Planets*, *127*(9), e2021JE007093.

Crumpler, L. S., Horgan, B. H. N., Simon, J. I., Stack, K. M., Alwmark, S., Gilles, D., ... Williams, N. R. (2023, October). In situ geologic context mapping transect on the floor of jezero crater from mars 2020 perseverance rover observations. *J. Geophys. Res. Planets*, *128*(10).

Farley, K. A., Stack, K. M., Shuster, D. L., Horgan, B. H. N., Hurowitz, J. A., Tarnas, J. D., ... Zorzano, M.-P. (2022, September). Aqueously altered igneous rocks sampled on the floor of jezero crater, mars. *Science*, *377*(6614), eabo2196.

Farley, K. A., Williford, K. H., Stack, K. M., Bhartia, R., Chen, A., de la Torre, M., ... Wiens, R. C. (2020, December). Mars 2020 mission overview. *Space Sci. Rev.*, *216*(8), 142.

Goudge, T. A., Mohrig, D., Cardenas, B. T., Hughes, C. M., & others. (2018). Stratigraphy and paleohydrology of delta channel deposits, jezero crater, mars. *Icarus*.

Goudge, T. A., Mustard, J. F., Head, J. W., & others. (2015). Assessing the mineralogy of the watershed and fan deposits of the jezero crater paleolake system, mars. *Journal of*.

Hayes, A. G., Corlies, P., Tate, C., Barrington, M., Bell, J. F., Maki, J. N., ... Winchell, K. (2021, February). Pre-flight calibration of the mars 2020 rover mastcam zoom (Mastcam-Z) multispectral, stereoscopic imager. *Space Sci. Rev.*, *217*(2), 1–95.

Hayes, A. G., Grotzinger, J. P., Edgar, L. A., Squyres, S. W., Watters, W. A., & Sohl-Dickstein, J. (2011, April). Reconstruction of eolian bed forms and paleocurrents from cross-bedded strata at victoria crater, meridiani planum, mars. *J. Geophys. Res.*, *116*(E00F21).

Horgan, B., Udry, A., Rice, M., Alwmark, S., Amundsen, H. E. F., Bell, J. F., III, ... Wiens, R. C. (2023, July). Mineralogy, morphology, and emplacement history of the maaz formation on the jezero crater floor from orbital and rover observations. *J. Geophys. Res. Planets*.

Kinch, K. M., Madsen, M. B., Bell, J. F., Maki, J. N., Bailey, Z. J., Hayes, A. G., ... Sørensen, A. N. (2020). Radiometric calibration targets for the Mastcam-Z camera on the mars 2020 rover mission. *Space Sci. Rev.*, *216*, 1–51.

Le Mouélic, S., Enguehard, P., Schmitt, H. H., Caravaca, G., Seignovert, B., Mangold, N., ... Civet, F. (2020, June). Investigating lunar boulders at the apollo 17 landing site using photogrammetry and virtual reality. *Remote Sensing*, *12*(11), 1900.

Maki, J. N., Gruel, D., McKinney, C., Ravine, M. A., Morales, M., Lee, D., ... Algermissen, S. (2020, November). The mars 2020 engineering cameras and microphone on the perseverance rover: A Next-Generation imaging system for mars exploration. *Space Sci. Rev.*, *216*(8), 137.

Mangold, N., Gupta, S., Gasnault, O., Dromart, G., Tarnas, J. D., Sholes, S. F., ... Williford, K. H. (2021, November). Perseverance rover reveals an ancient delta-lake system and flood deposits at jezero crater, mars. *Science*, *374*(6568), 711–717.

Maurice, S., Wiens, R. C., Bernardi, P., Caïs, P., Robinson, S., Nelson, T., ... Wong, K. W. (2021, April). The SuperCam instrument suite on the mars 2020 rover: science objectives and mast-unit description. *Space Sci. Rev.*, *217*(3), 47.

Over, J.-S. R., Ritchie, A. C., Kranenburg, C. J., Brown, J. A., Buscombe, D. D., Noble, T., ... Wernette, P. A. (2021). *Processing coastal imagery with agisoft metashape professional edition, version 1.6—structure from motion workflow documentation* (No. 2021-1039). US Geological Survey.

Paar, G., Mett, M., Ortner, T., Kup, D., & Kontrus, H. (2022, June). High-resolution real-time multipurpose tunnel surface 3D rendering. *Geomech. Tunn.*, *15*(3), 290–297.

Paar, G., Ortner, T., Tate, C., Deen, R. G., Abercrombie, P., Vona, M., ... Barnes, R. (2023). Three-Dimensional data preparation and immersive Mission-Spanning visualization and analysis of mars 2020 Mastcam-Z stereo image sequences. *Life Support Biosph. Sci.*, *10*(3), e2022EA002532.

Prepared by the Mars Sample Return Campaign Science Group (MCSG), Czaja, A. D., Zorzano, M.-P., Kminek, G., Meyer, M. A., Beaty, D. W., ... Members (2023, June). Report of the science community workshop on the proposed first sample depot for the mars sample return campaign. *Meteorit. Planet. Sci.*, *58*(6), 885–896.

Quantin-Nataf, C., Alwmark, S., Calef, F. J., & others. (2023). The complex exhumation history of jezero crater floor unit and its implication for mars sample return. *Journal of*.

Quinn, D. P., & Ehlmann, B. L. (2019, August). A PCA-based framework for determining remotely sensed geological surface orientations and their statistical quality. *Earth Space Sci.*, *6*(8), 1378–1408.

Ruoff, N. A., Deen, R. G., Pariser, O. (2023). Mars 2020 camera software interface specification (SIS) [Computer software manual]. JPL Doc ID: D-99960, Jet Propulsion Laboratory.

Schon, S. C., Head, J. W., & Fassett, C. I. (2012, July). An overfilled lacustrine system and progradational delta in jezero crater, mars: Implications for noachian climate. *Planet. Space Sci.*, *67*(1), 28–45.

Stack, K. M., Williams, N. R., Calef, F., 3rd, Sun, V. Z., Williford, K. H., Farley, K. A., ... Yingst, R. A. (2020, December). Photogeologic map of the perseverance rover field site in jezero crater constructed by the mars 2020 science team. *Space Sci. Rev.*, *216*(8).

Traxler, C., Ortner, T., Hesina, G., Barnes, R., Gupta, S., Paar, G., ... Willner, K. (2022, April). *The PRoViDE framework: Accurate 3D geological models for virtual exploration of the martian surface from rover and orbital imagery.* Wiley.

Wiens, R. C., Maurice, S., Robinson, S. H., Nelson, A. E., Cais, P., Bernardi, P., ... Willis, P. (2021). The SuperCam instrument suite on the NASA mars 2020 rover: Body unit and combined system tests. *Space Sci. Rev.*, *217*(1), 4.

Stratigraphic reconstruction and analysis of the delta remnant Kodiak in Jezero Crater, Mars

C. D. Tate[1], A. H. Hayes[1], O. A. Kanine[2], S. Gupta[3], G. Caravaca[4], G. Paar[5], S. Le Mouélic[6], C. Traxler[7], J.W. Rice, Jr.[8]

[1]Cornell University, Department of Astronomy and Planetary Science, Ithaca, NY, USA
[2]California Institute of Technology Division of Geological and Planetary Sciences, Pasadena, CA, USA
[3]Imperial College London, Department of Earth Science and Engineering, London, UK
[4]Institut de Recherche en Astrophysique et Planétologie, CNRS, Université de Toulouse, CNES, France
[5]Joanneum Research, Institute for Digital Technology, Graz, Austria
[6]CNRS Délégation Bretagne et Pays de Loire, Nantes, France
[7]VRVis Zentrum für Virtual Reality und Visualisierung Forschungs-GmbH, Wien, Austria
[8]Arizona State University, School of Earth and Space Exploration, Tempe, AZ, USA

Key Points:

- We present a digital 3D reconstruction of Kodiak sourced from over 400 images taken by the Mars 2020 Perseverance Rover.
- This science-grade model enables precise geometric measurements of Kodiak's strata that are essential for its geological interpretation.
- Kodiak's has at least three units, of which two have bedding layers with widely varying strikes that suggest fluvial processes.

Corresponding author: Christian Tate, `cdt59@cornell.edu`

Abstract

We analyze Kodiak, an eroded delta remnant in Jezero Crater, Mars, using several hundred images from the Mastcam-Z and SuperCam instruments on the Mars 2020 Perseverance Rover. We create a high-accuracy digital terrain model to measure Kodiak's stratigraphic layers, which we divide into three units and characterize individually. While each unit possesses geometries interpreted as consistent with a Gilbert-style delta formation, the older units exposed on Kodiak's north to northeast sides include more complex layered structures with azimuthally varying foresets. We compare Kodiak's northeast foresets with the clinoforms of Whale Mountain, an outcrop exposed in the Western Jezero Delta scarp, and show similar azimuthally varying foresets. The stratigraphic analysis presented herein (strike and dip, unit thickness, etc.) will help test and refine detailed sedimentological hypotheses for the formation and evolution of the Jezero delta. Our 3D reconstruction and measurements enable unprecedented precision to evaluate depositional models and advance geological interpretation.

Plain Language Summary

We examine an ancient delta remnant (named Kodiak) in Mars' Jezero Crater using images from the Perseverance Rover's Mastcam-Z and SuperCam. We created a detailed digital terrain model to analyze its layered structure, dividing it into several distinct units. Each unit showed features typical of a Gilbert-style delta, but the older layers on Kodiak's north and northeast sides were more complex. We compared these layers with similar formations. Our analysis includes detailed measurements of the layers' orientation and thickness and will refine our understanding of how the Jezero delta formed and evolved. This work required close collaboration among different teams operating the rover and its instruments. Despite camera calibration and image correlation challenges, our 3D models provide a precise view of Kodiak's geology, offering new insights into the Martian landscape.

1 Introduction

Kodiak is an 80 m tall and 250 m wide butte located less than a kilometer south of the Jezero Western fan scarp (Mangold et al. (2021)). The Western Jezero Delta, radiating from Neretva Vallis, was once likely connected to several hills or knobs scattered within a 10 km radius of the Neretva Vallis inlet before undergoing significant erosion (Schon et al. (2012); Goudge et al. (2015)). One such remnant, Kodiak, was continuously visible to the Perseverance rover throughout the first two years of the Mars 2020 mission and contains sedimentary strata that chronicle a portion of the depositional history of Jezero Crater and have been interpreted as indicators of an ancient lake environment (Mangold et al. (2021); Farley et al. (2022)). Kodiak's exposed bedforms (Fig. 1) were fortunately perpendicular to the rover traverse for this portion of the mission and, therefore, in a favorable alignment for rover-based imaging and long-baseline stereo reconstruction. Herein, we describe our new application of structure from motion (SfM) to over 400 images to generate a three-dimensional (3D) model of Kodiak's exposed stratigraphy. We use this Digital Terrain Model (DTM) to determine stratigraphic relationships in the Kodiak deposit and interpret the strike and dip of exposed beds in the context of a typical Gilbert-style delta.

Visualizing and characterizing geological features in three dimensions is crucial for their complete interpretation, and the lack of realistic and flexible rendering is a significant challenge for exploring remote, human-inaccessible locations like Mars. Recently, planetary geomorphologic studies have begun using Structure-from-Motion photogrammetry (SfM) to create 3D Digital Terrain Models (DTMs) of Martian terrains, such as the Kimberley outcrop (Caravaca et al. (2020)) and the Glen Torridon region (Caravaca et al. (2022)) in Gale Crater, that can be visualized in virtual reality (VR) environments for a more immersive and realistic experience of the terrain with its spatial relationships (e.g., Caravaca et al. (2020)). More traditionally, stereo photogrammetric processes are used to create DTMs on which researchers perform geometric analysis (e.g., Barnes et al. (2018); Banham et al. (2018, 2022); Traxler et al. (2022); Paar et al. (2023)) using software such as PRo3D (Traxler et al. (2022)) to obtain geometric measurements including strike and dip for each layer. While VR-compatible DTMs offer a rich visual context for qualitative geological interpretation (Barnes et al. (2018)), they cannot reach their full scientific potential without permitting quantitative analysis of layer thickness, dip angles, strike azimuths, and other geometric properties. Herein, we discuss a process that combines the immersive experience of the VR-compatible DTMs with the quantitative analysis of traditional DTMs to analyze Kodiak.

Early in its mission, the Mars 2020 Perseverance Rover documented Kodiak's East and North faces from various perspectives (Figs. 1 and 2). We use the data collected during this campaign to create a high-resolution DTM optimized bot for immersive VR environments and stratigraphic analysis tools such as PRo3D. We then use the model to measure the dimensions and orientations of various bedding packages observed in Kodiak's exposed stratigraphy. We build on the methodologies of prior studies (Caravaca et al. (2020); Barnes et al. (2018); Banham et al. (2018)) by combining the improved accuracy of multi-view SfM photogrammetry with a complete 3D analysis workflow to constrain Kodiak's stratigraphic relationships and interpret the strike and dip of exposed bedding layers in the context of a typical Gilbert-style delta. The DTMs, rendered orthographic mosaics, and plane measurements provided herein are used in other studies (Caravaca et al. and Kanine et al., both in this issue). These papers go beyond our present research and evaluate specific sedimentologic scenarios to explain our observations and measurements.

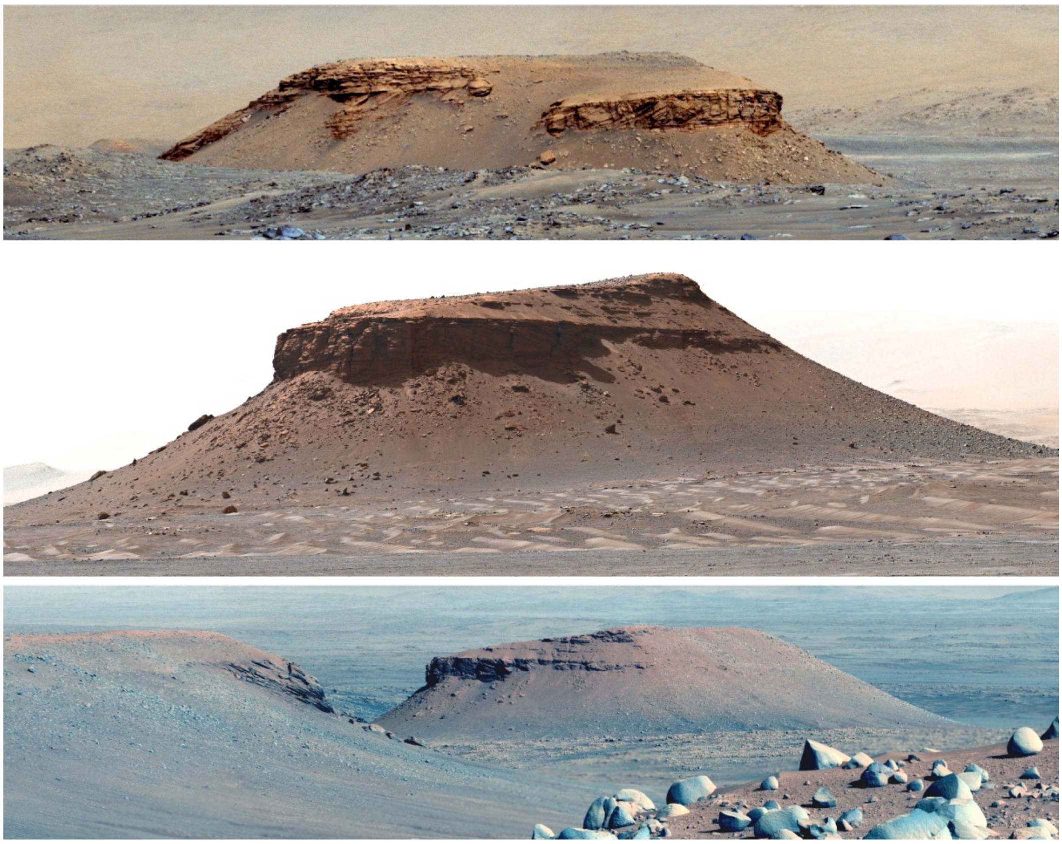

Figure 1. Mastcam-Z mosaics of Kodiak from several perspectives: (a) showing the eastern outcrops on Sol 83 (earth date), (b) northern outcrops on Sol 409 (April 14, 2022), and (c) the northwest side from Sol 753 (April 3, 2023) after climbing the delta and gaining 130 m of elevation. The structure on the left of (c) is the southern side of Whale Mountain. Image credits: NASA/JPL/MSSS/ASU.

2 Data

Our process uses radiance-calibrated (RAD) images taken from Sol 4 to Sol 580 (March 1, 2021 to Oct. 7, 2022) with two science instruments on the Mars 2020 Perseverance rover: the Mastcam-Z multispectral stereo imagers (Bell et al. (2021); Hayes et al. (2021); Kinch et al. (2020)) and SuperCam's Remote Micro-Imager (RMI) Maurice et al. (2021). The SuperCam RMI has a field of view (FOV) of about 1° with a pixel instantaneous field of view (IFOV) of 10µrad (Maurice et al. (2021); Wiens et al. (2021)). Although RMI images have more resolving power than the Mastcam-Z's, even at their highest zoom of 110 mm focal length (6° FOV and 67µrad IFOV, Hayes et al. (2021)), this comes at the expense of a restricted FOV. The best Mastcam-Z resolution on Kodiak is from a distance of 480 m, where its horizontal pixel scale is 3.3 cm. Kodiak's eastern outcrops were imaged from farther distances (1.9-3.2 km), with a best pixel scale of 13 cm.

This Kodiak imaging campaign required coordination between SuperCam, Mastcam-Z, and rover operations teams. As Perseverance progressed along its route and new perspectives of Kodiak came into view, the Mars 2020 science team requested observations to fill gaps in the butte's coverage. The imaging resolution of Kodiak varies across the campaign according to Perseverance's traverse; Table 1 summarizes Kodiak's Mastcam-

Z dataset and gives the estimated values for the resolution of each region of Kodiak captured. The reconstructed model shown in Fig. 3 uses over 400 Mastcam-Z images of Kodiak and its surrounding terrain along the rover traverse (shown in Fig. 2). Additional structural and textural detail comes from 52 SuperCam RMI images captured from six unique locations (Table S2).

The first 400 sols of the Mars 2020 mission included the Crater Floor Campaign (Horgan et al. (2023)), during which Perseverance imaged Kodiak's eastern face from azimuths between 65° to 102° and distances between 1.8 km and 2.6 km. Images from the Delta Front and Sample Depot campaigns Prepared by the Mars Sample Return Campaign Science Group (MCSG) et al. (2023) on sols 400-715 saw Kodiak's northern face from -36°N to 19°N azimuth and between 0.5 and 1.1 km distance and from an average of 32 m higher elevation than previous campaigns. The relative illumination and viewing geometries of Kodiak and the rover determined the most scientifically valuable time of day to take the images. The best images of eastern Kodiak in the first 400 sols were taken in morning lighting, while the best images of the often highly shadowed northern outcrops had evening illumination. We do not use images taken after Sol 700 because they have lower spatial resolution and do not significantly expand the coverage of Kodiak's most exposed outcrops.

Three dual-instrument sequences taken on Sols 63, 248, and 580 form the core of this dataset. Together, these images document about two-thirds of Kodiak. This region includes most of Kodiak's exposed outcrops above its wide scree and talus skirt judging from orbital views (Fig. 2).

3 Terrain Reconstruction

We use structure from motion (SfM) with the Mastcam-Z and SuperCam images (listed in supplementary Tables S1 and S2) to reconstruct the high-resolution digital terrain model (DTM) shown in Fig. 3. This model is viable and downloadable from Sketchfab from the following link: https://skfb.ly/oCyI8. We pre-processed each PDS image data product with a Python script that opened, transformed, and saved the images and camera model information in formats compatible with Agisoft Metashape. The localized exterior camera models are the primary metadata we extract from the PDS headers. These encode the image's position and orientation in a coordinate system compatible with the SfM software. This code used to perform this analysis is available on GitHub: https://github.com/cdt59/MPPP.

3.1 Long-baseline Stereo and Structure from Motion (SfM)

Long-baseline stereo techniques have precedence on Mars rover missions for capturing high-resolution topographic data (Caravaca et al. (2021)). These techniques typically involve capturing stereo pairs of images from two distinct but well-characterized positions, often separated by large distances relative to the target, to reconstruct the 3D geometry of the terrain. Such methods have been beneficial for navigational and scientific documentation, as they provide a quick way to obtain depth information from a scene (Maki et al. (2020); Bell et al. (2021)). However, traditional long-baseline stereo techniques often rely on single-pair stereo matching, which can be susceptible to calibration, alignment, and localization errors (Hayes et al. (2011); Barnes et al. (2018)).

In contrast, our approach employs Structure from Motion (SfM) as implemented in Agisoft Metashape Professional, which offers several advantages (Agisoft (2019); Le Mouélic et al. (2020); Over et al. (2021); Caravaca et al. (2021); Bistacchi et al. (2022); Paar et al. (2023)) as well as industrial applications (Paar et al. (2022)). SfM uses multiple images from different viewpoints to create a more self-consistent Digital Terrain Model (DTM). This method minimizes errors globally across the dataset by comparing tie points in one image to every other overlapping images, solving for each image's highest confidence depth map (Agisoft (2019); Over et al. (2021); Caravaca et al. (2021)). The resulting 3D model is more accurate and comprehensive because it minimizes camera model errors over all images and control points. Thus, while long-baseline stereo provides a robust but sometimes limited snapshot of the Martian terrain, our SfM approach creates a more detailed and accurate 3D reconstruction.

3.2 Rover Localization

Perseverance operations align each end-of-drive location with a Mars 2020 basemap and make these rover waypoints available for science analysis. The Mars 2020 basemap is made from a mosaic of orbital HiRISE images and has a resolution of about 25 cm (Stack et al. (2020); Farley et al. (2020)). Accurate rover and camera localization are required to generate precise models at their location, orientation, and scale. The estimated position and orientation of the image are made in Site Frame as obtained from the JPL localization process (Calef et al. (2023); Crumpler et al. (2023); Ruoff, N. A., Deen, R. G., Pariser, O. (2023)) to ensure that the SfM algorithm has the best available initial camera models for correctly triangulating points in space, thereby generating a reliable and high-fidelity 3D model. Inaccurate localization data can introduce errors in the reconstructed geometry, leading to distortions or misalignments in the resulting DTM. Moreover, precise localization allows for effectively merging data from different imaging campaigns or instruments, such as Mastcam-Z and SuperCam's Remote Micro-Imager, into a single, coherent model. This is particularly crucial when the model aims to capture complex geological features like the strata exposed at Kodiak.

3.3 Reconstruction Error

Two sources of error dominate the accuracy and precision of 3D reconstructions: uncertainties in the geometric camera model and range errors originating from correlation uncertainties. Although the Mars 2020 cameras are robustly calibrated in the rover coordinate system (Maki et al. (2020); Hayes et al. (2021)), the absolute camera positions are less constrained in the Mars-fixed coordinate system in which the vehicle estimates its position and orientation as it drives through the terrain. This introduces projection errors that structure from motion mitigates by optimizing camera parameters in a global control network. These projective errors are distinct from a second source: range error, the precision with which a stereo pair of images can correlate features and estimate their position in space with triangulation. Range error is in the line-of-site or range direction and increases quadratically for a fixed stereo base length. Because range error only quantifies the sub-pixel correlation between two stereo images, it is not a valid estimate of a model's overall reconstruction quality. Nevertheless, we assume that range errors are the primary source of non-correlated errors. As such, range error limits the relative position of points on the model surface for plane-fitting strike and dip analysis.

The theoretical range error is a standard but limited measure of reconstruction error. Similar to how imaging resolution estimates the precision of the image projection onto the model, the range error estimates the precision in the third axis (i.e., the range axis, which is orthogonal to the image's line and sample axes). Each well-characterized stereo pair can yield a digital terrain model (DTM) with a pixel-by-pixel accuracy determined by the camera properties and the relative geometry of imaging locations and the terrain. We estimate range errors for this model are comparable to the pixel scale, which is 3.3 and 13 cm for Kodiak's north and east faces, respectively (Table 1). Further details about our methodology for estimating the 3D reconstruction error are in S2 of the online supplementary materials.

Table 1. Summary of the Mastcam-Z observations of Kodiak, which we separate into four azimuth ranges relative to Kodiak. These are limited to Mastcam-Z sequences taken at its highest resolution zoom level at 110mm.

	East	**Northeast**	**North**	**Northwest**
sol range	004 – 275	382 – 388	409 – 711	750 – 756
imaging locations[1], total	23	3	11	3
imaging locations[1], used[2]	8	3	6	0
SuperCam locations[3], total	3	0	3	0
preferred time of day [4]	morning	morning	afternoon	evening
local mean solar time	7:58 – 11:38	8:10 – 9:36	10:04 – 16:00	11:46 – 16:03
local mean solar time, average	10:20	9:10	13:20	14:30
range[5] [km]	1.8 – 2.4	2.5 – 3.2	0.48 – 1.1	2.4 – 2.5
range[5], average [km]	2.2	2.8	0.71	2.5
elevation [m]	-5.3 – 1.8	-1.3 – 2.2	21 – 48	127 – 133
elevation, average [m]	0.0	0.3	32	130
azimuth[6] [°North]	84° – 102°	64° – 79°	324° – +19°	315° – 320°
azimuth[6], average [°North]	92°	73°	348°	318°
pixel scale, average [cm/pixel]	15	19	4.8	17
pixel scale, best [cm/pixel]	12	17	3.2	16
range error[7], average [cm]	140	98	4.4	160
range error[7], best [cm]	35	24	2.2	55

[1] See Table S1 or the online spreadsheet for details on each Mastcam-Z sequence.

[2] The values below are only for used sequences. See Table S1.

[3] This is the total number of SuperCam RMI sequences taken in each region. See Table S2 for details. All other information in this table is for the Mastcam-Z sequences.

[4] The Sun's incidence angle is important for capturing the fine details on Kodiak because of its many vertical outcrops. The preferred time of day is when the outcrop is best illuminated, which happens when the Sun is approximately behind the camera.

[5] We calculate range as the distance from the rover's location to a reference point in Kodiak (the center of curvature of Unit 1, which we assume to be 2335 m West, 244 m South, and 50 m above the O.E.B. landing site). See the downloadable supplementary spreadsheet for each imaging location's relative Northing, Easting, and Elevation.

[6] We calculate azimuth as the clockwise angle from North to a reference point in Kodiak (the center of curvature of Unit 1).

[7] See section S2 for how we calculate range error and recommend interpreting it.

3.4 Geometric measurements

We inspect and annotate the model using the Planetary Robotics 3D Viewer software abbreviated PRo3D (Barnes et al. (2018); Traxler et al. (2022)). The PRo3D software imports DTMs and provides several annotation tools that we use to trace the outcrop layers and measure their strike and dip angles. PRo3D uses the plane-fitting algorithm to calculate layer orientation and error. This algorithm uses principal component analysis (PCA) described in (Quinn & Ehlmann (2019)) to constrain layer geometry and estimate measurement uncertainty. Additional information about PRo3D and annotation files used for our measurements can be found in S3 and S4. The XYZ points extracted from our layer tracings are available in the supplementary materials for future researchers who want to use alternative methods for determining layer orientation.

4 Results

We divide the stratigraphy of Kodiak butte into three units, each containing inclined beds bounded by sub-horizontal beds and separated by truncation surfaces. We adopt the naming convention used in Caravaca et al. (this issue) and describe Units 0, 1, and 2 in stratigraphic order, as shown in Fig. 3. Table 2 lists each unit's average sequence thickness, dip, and strick measurements.

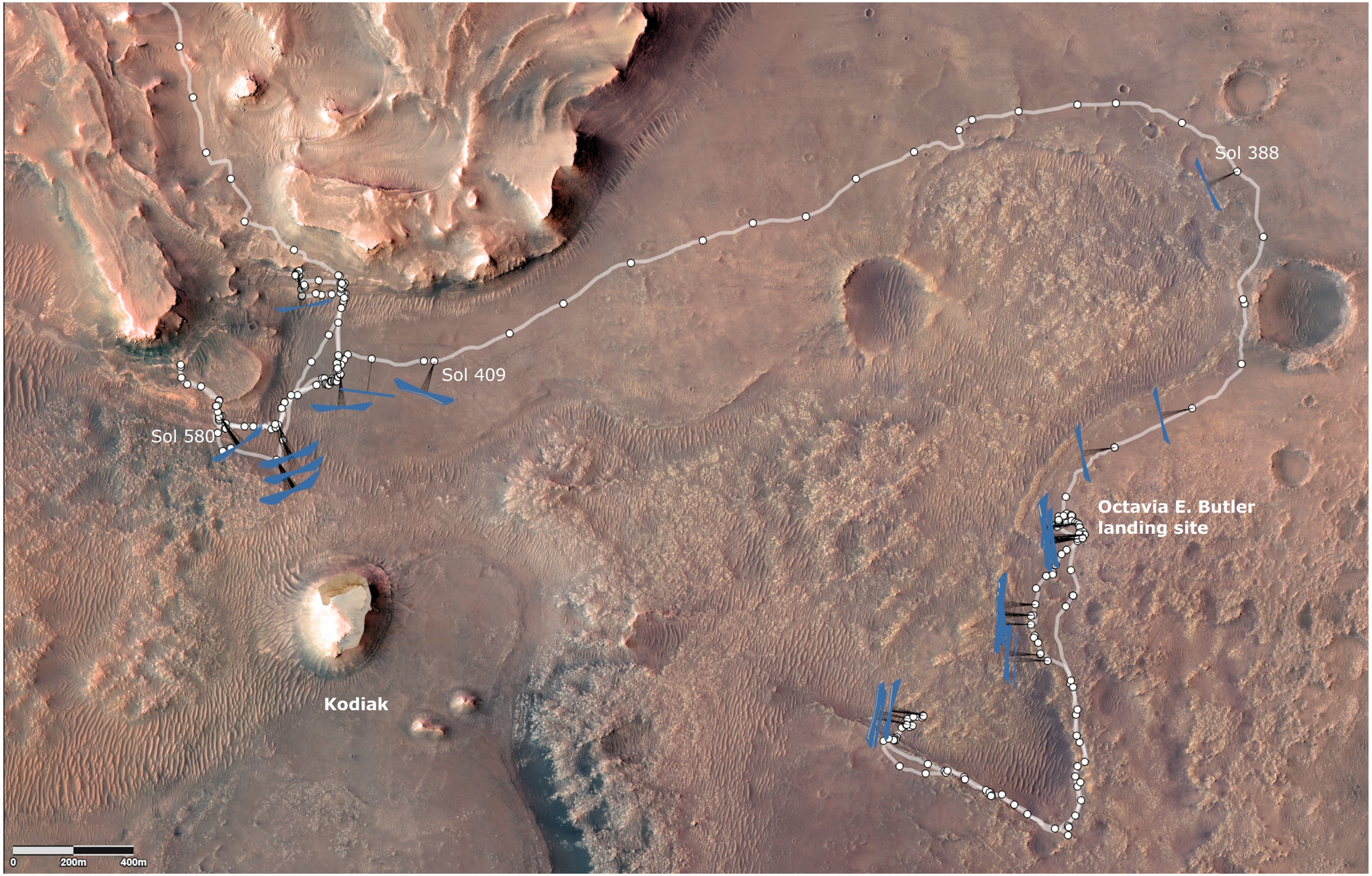

Figure 2. The Mars 2020 basemap of the Jezero Crater (primarily made from HiRISE mosaics) and the traverse of the Perseverance rover for the first 715 Sols of the Mars 2020 mission. The white dots show the locations where the rover stopped to take images, and the blue and black symbols show the positions and pointing of the Mastcam-Z images used to reconstruct Kodiak.

4.1 Unit 0

Unit 0 outcrops on the northwest flank of Kodiak butte. Scree covers its lower layers, making it the only unit without visible bottomsets. Unit 0 consists dominantly of variably inclined strata that extend laterally for about 60 m, as measured from our SfM model. It shows average and maximum thicknesses of 2.5 and 3.7 m, respectively. A convex-up sedimentary body in the center of Unit 0 is 6 m wide and 1 m high and has inclined layers on both flanks. Overlying this convex-up feature, we measure a range of dips between 15 to 25°, predominantly towards the northeast, at 35°N. At the east side of the outcrop, Unit 0's foresets are truncated by onlapping inclined layers of Unit 1. On top of the inclined layers, a sub-horizontal erosion surface separates them from sub-horizontal topset beds. These topsets appear to be stratigraphically equivalent to Unit 1's topset.

4.2 Unit 1

Unit 1 outcrops Kodiak's northeast flank. The lower part consists of over 5 m of sub-horizontal strata that dip $\sim 5°$ approximately to the south $\sim 179°$N. Another apparent outcrop of Unit 1's sub-horizontal strata occurs lower on the northeast corner of the butte. These layers appear to be in place, indicating about 10 m of sub-horizontally stratified rocks within the lower part of Unit 1.

The inclined beds of Unit 1 extend over 160 m from the middle of Kodiak's northern face to the middle of its eastern face. These layers have a range of dip azimuths between 180°N and $\sim 250°$N at Unit 1's southern and western extents, respectively. The inclined layers on the northwest side of Unit 1 onlap the inclined layers of Unit 0. At this interface between Units 1 and 0, the bedding dip azimuths are approximately opposite. Cobble-sized clasts (0.1-0.2 m in diameter) are embedded in Unit 1 close to this boundary, and these rounded grey clasts stand out against the nominal red appearance of Kodiak's strata. The inclined strata in the rest of Unit 1's northern exposure show a 6-7.2 m thick section of sigmoidal layers. Although the dip and strike geometries are complex to constrain on this flat outcrop face, they are consistent with dip azimuths to the southwest (Fig. 3).

Kodiak's strata at its northeast corner (or "nose") appear to be plunging into the outcrop. This is the boundary between Unit'1 north and east inclined layers, which we characterize as the point of greatest dip azimuth divergence. The outcrop at this crucial location is weathered, crumbly, and only obliquely imaged in shadow. Despite these difficulties, our reconstructed model reveals a doming pattern that is not apparent from the separate inspection of the original images. The inclined beds dip in divergent directions on both sides of this junction. Unit 1 North dips towards $\sim$ 230°N, and Unit 1 East dips towards 180°N. The latter contains the tallest and steepest inclined beds measured on Kodiak, at about 9 m tall and 40° dip towards the south. At the southern extent of Unit 1, the inclined beds shallow to dip angles of about 10°.

The upper sub-horizontal layers appear equivalent across both sides of Unit 1's east-north junction and with the topsets of Unit 0. However, on the southern end of Unit 1, the truncation surface appears to fade as the overlying strata drapes more continuously with the shallowly dipping inclined beds below.

4.3 Unit 2

Unit 2's lower sub-horizontal layers appear continuous with Unit 1's inclined beds, although scree covers large areas separating these two units. This package is up to 10 m thick, making it the thickest sub-horizontal part of Kodiak. This outcrops in the middle of Unit 2 and at its southern extent. The inclined beds of Unit 2 range between 2 to 5.6 m thick with an average of 4 m. Like Unit 1, the southernmost beds are shallow to about 10° dip. Unlike Unit 1, however, all the inclined strata dip towards a consistent azimuth of 135°N.

The sub-horizontal layers overlying Unit 1 are inclined at an average dip of 4.1° towards the same azimuth of 134°N. At the interface of the inclined strata and overlying sub-horizontal strata, scouring and crossbedding are observed. Unit 2 also outcrops on Kodiak's north side above Units 0 and 1. Here, the strata show cross-bedding similar to the equivalent layers on Kodiak's southern end. However, the orientation of these exposures to their probable dip directions is not favorable for reliable measurements of dip and strike.

4.4 Unit 3

Unit 3 is a deposit of boulders and cobbles overlying Unit 2's topsets. The most visible boulders have 0.5 m diameters, and we measure the largest as wide as 2 m. There does not appear to be any strata in Unit 3; hence, we do not include it in Table 2.

Table 2. Measurements on the 3D reconstruction of Kodiak. These give the horizontal scale of each major sequence, the number of strike and dip measurements on suitable outcrops, and their average values of dip angle and azimuth. After projecting each vector into the horizontal plane, we calculated the average azimuth values. Kodiak is divided into three units, as illustrated in Fig. 3, with Unit 1 further differentiated between east and north to highlight its variation in dip azimuth directions.

	Unit 0	**Unit 1, North**	**Unit 1, East**	**Unit 2**
Mastcam-Z resolution [cm]	3.3	3.3	18	13
outcrop exposure width [m]	60	80	100	120
topset height [m]	2.0	2.0	2.5	9.7
topset measurements	3	9	5	48
topset dip [°]	5.7	4.9	5.4	4.1
topset azimuth [°N]	342	347	232	134
foreset height [m]	2.5	5.9	7.7	4.0
foreset max height [m]	3.7	7.2	9.0	5.6
foreset measurements	11	29	40	21
foreset dip [°]	18.8	29.2	28.1	27.0
foreset azimuth [°N]	35	229	180	135
bottomset height [m]	-	>3	>2	10
bottomset measurements	-	1	9	3
bottomset dip [°]	-	∼8	4.5	∼6.6
bottomset azimuth [°N]	-	∼160	179	∼148

5 Discussion

Our 3D digital outcrop model of Kodiak butte provides an unprecedented opportunity to measure the quantitative geometry of its exposed layers. In Unit 2, Kodiak shows structures consistent with the previously proposed Gilbert delta model (Mangold et al. (2021)), with the central section comprising foreset beds that smoothly transition into bottomset strata at their base and overlying topset strata that abruptly terminate the foresets at their top. The foreset beds in Unit 2 show a consistent dip of 30° to the southeast, while the topsets and bottomsets dip about 3-8° in the same direction. These observations alone suggest a Gilbert-style delta depositional model for Kodiak with the delta lobe prograding basinward from the Neretva Valis inlet to the southeast at 140°N.

Within Units 0 and 1, however, the layers appear to have a more complex structure than the typical Gilbert-style deltaic succession shown in Unit 2. Not only does Unit 1's bedding azimuths change throughout the exposure, but these dip angles are also the

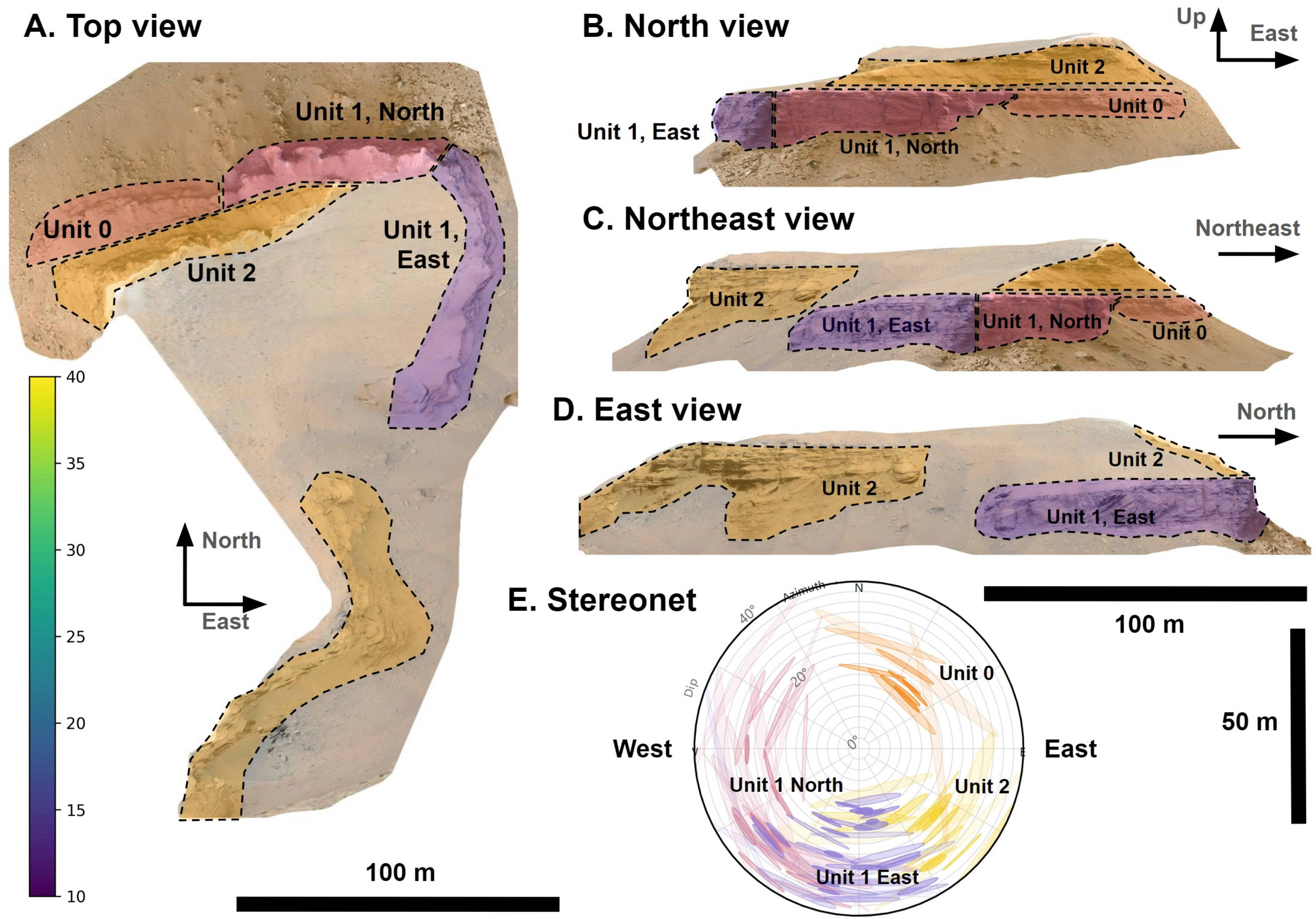

Figure 3. Rendered images of Kodiak's 3D reconstruction. Dashed lines show the approximate boundaries of Kodiaks' three stratigraphic units. (a) is a vertical orthographic projection of Kodiak with superimposed strike and dip symbols showing the dip magnitudes and azimuth orientations for each unit characterized in this study. The side views of Kodiak are orthographic projections (b) from the north, azimuth $0°N$, (c) from azimuth $45°N$, and from the east, azimuth $90°N$. (e) Stereonet of the foreset strike and dip measurements with their error ellipses Quinn & Ehlmann (2019).

steepest measured at Kodiak. Foreset strata in Units 0 and 1 indicate different accretion directions across a small lateral extent (∼50 meters), indicating deposition within narrow, overlapping delta lobes (Caravaca et al., this issue). The foresets of unit 1 also have the greatest thickness on Kodiak, with a 9.0 m maximum foreset thickness on its eastern face. As seen in Table 2, these vertical heights are considerably larger than Units 0 and 2. These measurements on Units 0 and 1 reveal geometrical complexity that may challenge a deltaic depositional hypothesis for Kodiak (see Kanine et al., this issue).

5.1 The narrow deltaic lobe interpretation

Unit 1 contains foreset beds that diverge ∼60° in azimuth over a horizontal distance of less than 50 m. This suggests that the original geometric planform of the foreset-containing sedimentary body was a relatively narrow lobate, convex-up form. Meanwhile, Unit 0 has irregular structures and an average dip direction of foreset beds opposite to Unit 1, indicating that it represents a different sedimentary body that accreted in an other direction. The northeast "nose" of Kodiak's Unit 1 could be a delta lobe that prograded to the southwest. Although its ∼50 m radius of curvature is narrow for a delta lobe, this scale is consistent with a relatively young lobe (Barrett et al. (2020)).

5.2 Comparisions to the main Western delta front

The leading Western delta front contains foreset structures similar to those observed at Kodiak. Whale Mountain (SF model), for instance, is the closest part of the Western Delta to Kodiak. Fig. S4 shows Whale Mountain's dip directions and how their radius of curvature has a similar ∼50 m scale as the diverging clinoforms we measured on the northeast side of Kodiak's Unit 1. While Kodiak's outcrop is neither well-preserved (highly weathered and degraded) nor well-imaged (in shadow and foreshortened by its off-normal orientation relative to the imaging direction), Whale Mountain presents a clean, vivid outcrop. Mastcam-Z imaged it on Sol 614 in optimal illumination and 1 cm/pixel (more than three times finer resolution than the best on Kodiak). Images from the delta top campaign imaged the western side of Whale Mountain (Sols 753, 756, 762), and show that its dip azimuths diverge a total of ∼180°. This is a more extreme dip azimuths divergence than the ∼50° measured on Kodiak. If there is a valid comparison between the narrow delta lobe interpretation of Kodiak Unit 1 and the similar structure of Whale Mountain, then studying the latter could be essential to understanding Kodiak.

Other structures on the delta front have foresets with vertical outcrops of over 20 m, which are far taller than Kodiak's maximum foreset height of 10 m. These locations on the delta front (in order of closest to farthest from Kodiak) are Mount Juhle (imaged on Sol 614, 625) (https://skfb.ly/ozZ9P), Franklin Cliff (Sol 696, 704) https://skfb.ly/oMpYF), and finally the Minors Castle and Morro Rock area (Sol 397, 398) on the easternmost extent of the Western Delta https://skfb.ly/oJp8U). Franklin Cliff is especially interesting for its preserved contact between foresets and topsets. These and other structures on Jezero's Western delta front are analyzed by Gupta et al. (this issue). Future studies should examine the deltaic environment required to produce horizontally curving foresets and how deltaic advancement could be toward the southwest, and compare these findings with evidence in the Western delta.

5.3 Comparisions to other delta rements

Two other remnants named Dragonera and Cabrerae stand southeast of Kodiak. Although smaller and more weathered than Kodiak, Cabrere contains outcrops southwest dipping foresets and bottomsets similar to those seen on Kodiak (albeit ∼50 meters lower elevation). Dragonera and the more distal remnants, such as Santa Cruz (images on Sols 36, 123) and Isle Royale (Sol 676) to the east and Pilot Pinnacle (Sol 128) to the south, are smoother and do not have analogous outcrops. It is unknown what causes this range of geomorphic expressions (Goudge et al. (2018); Quantin-Nataf et al. (2023)), but we find inclined beds resembling foresets only on the two remnants closest to the Western Delta.

6 Conclusion

We present a detailed 3D digital outcrop model of the Kodiak butte created from the fusion of hundreds of Perseverance Rover images. Stratigraphic analysis of the resulting DTM expands upon previous interpretations of Kodiak as deposits from a Gilbert-style delta with quantitative measurements. Our study shows the foreset strike azimuths change systematically over Kodiak's north and northeast outcrops. The depositional environments preserved in Kodiak are related to the enormous Western Delta fan, and investigating Kodiak can advance our understanding of Jezero's other deltaic structures throughout the crater floor.

7 Data Availability Statement

This study utilizes data from Mars rover imaging, which are archived and accessible through the Planetary Data System (PDS). The end data products derived from these images and our processing are included in the supplementary materials of this article for ease of reference and use. In adherence to the FAIR Data principles, we ensure that our data is Findable, Accessible, Interoperable, and Reusable. Descriptions and access instructions for all other utilized data and software tools, which are publicly available, and can be found in (Tate, 2023).

Acknowledgments

The Mars 2020 Mastcam-Z and SuperCam teams were tremendously influential in collecting and formatting these images. Another thanks to NASA's Planetary Data System (PDS), from which all the data used in this study are publicly available. The JPL Mars 2020 Localization Team provided the localization and pose for each Perseverance rover end-of-drive location. Joanneum Research and VRVis receive funding from the Austrian Research Promotion Agency, ASAP-18 Project 892662 "Mars-3D". VRVis is funded by BMK, BMAW, Styria, SFG, Tyrol, and Vienna Business Agency in the scope of COMET - Competence Centers for Excellent Technologies (879730), which FFG manages.

References

Agisoft, L. L. C. (2019). Agisoft metashape user manual: Professional edition. *Version*.

Banham, S. G., Gupta, S., Rubin, D. M., & others. (2022). Evidence for fluctuating wind in shaping an ancient martian dune field: The stimson formation at the greenheugh pediment, gale crater. *Journal of*.

Banham, S. G., Gupta, S., Rubin, D. M., Watkins, J. A., Sumner, D. Y., Edgett, K. S., ... Vasavada, A. R. (2018, June). Ancient martian aeolian processes and palaeomorphology reconstructed from the stimson formation on the lower slope of aeolis mons, gale crater, mars. *Sedimentology*, *65*(4), 993–1042.

Barnes, R., Gupta, S., Traxler, C., Ortner, T., Bauer, A., Hesina, G., ... Tao, Y. (2018, July). Geological analysis of martian rover-derived digital outcrop models using the 3-D visualization tool, planetary robotics 3-D viewer-PRo3D. *Earth Space Sci.*, *5*(7), 285–307.

Barrett, B. J., Gawthorpe, R. L., Collier, R. E. L., Hodgson, D. M., & Cullen, T. M. (2020, February). Syn-rift delta interfan successions: Archives of sedimentation and basin evolution. *Depositional Rec.*, *6*(1), 117–143.

Bell, J. F., 3rd, Maki, J. N., Mehall, G. L., Ravine, M. A., Caplinger, M. A., Bailey, Z. J., ... Wolff, M. J. (2021, February). The mars 2020 perseverance rover mast camera zoom (Mastcam-Z) multispectral, stereoscopic imaging investigation. *Space Sci. Rev.*, *217*(1), 1–40.

Bistacchi, A., Mittempergher, S., & Martinelli, M. (2022, April). *Digital outcrop model reconstruction and interpretation.* Wiley.

Calef, F. J., Parker, T. J., Schroeder, J., Williams, N., & Golombek, M. P. (2023, March). *Spatial products and services for the mars2020 perseverance rover* (Vol. 2806). ui.adsabs.harvard.edu.

Caravaca, G., Le Mouélic, S., Mangold, N., Jonas, L., Laetitia, L. D., & Marion, M. (2020, March). 3D digital outcrop model reconstruction of the kimberley outcrop (gale crater, mars) and its integration into virtual reality for simulated geological analysis. *Planet. Space Sci.*, *182*, 104808.

Caravaca, G., Le Mouélic, S., Rapin, W., Dromart, G., Gasnault, O., Fau, A., ... Lanza, N. L. (2021, October). Long-distance 3D reconstructions using photogrammetry with curiosity's ChemCam remote Micro-Imager in gale crater (mars). *Remote Sens. (Basel)*, *13*(20), 4068.

Caravaca, G., Mangold, N., Dehouck, E., Schieber, J., Zaugg, L., Bryk, A. B., ... Lanza, N. L. (2022, September). From lake to river: Documenting an environmental transition across the Jura/Knockfarril hill members boundary in the glen torridon region of gale crater (mars). *J Geophys Res Planets*, *127*(9), e2021JE007093.

Crumpler, L. S., Horgan, B. H. N., Simon, J. I., Stack, K. M., Alwmark, S., Gilles, D., ... Williams, N. R. (2023, October). In situ geologic context mapping transect on the floor of jezero crater from mars 2020 perseverance rover observations. *J. Geophys. Res. Planets*, *128*(10).

Farley, K. A., Stack, K. M., Shuster, D. L., Horgan, B. H. N., Hurowitz, J. A., Tarnas, J. D., ... Zorzano, M.-P. (2022, September). Aqueously altered igneous rocks sampled on the floor of jezero crater, mars. *Science*, *377*(6614), eabo2196.

Farley, K. A., Williford, K. H., Stack, K. M., Bhartia, R., Chen, A., de la Torre, M., ... Wiens, R. C. (2020, December). Mars 2020 mission overview. *Space Sci. Rev.*, *216*(8), 142.

Goudge, T. A., Mohrig, D., Cardenas, B. T., Hughes, C. M., & others. (2018). Stratigraphy and paleohydrology of delta channel deposits, jezero crater, mars. *Icarus*.

Goudge, T. A., Mustard, J. F., Head, J. W., & others. (2015). Assessing the mineralogy of the watershed and fan deposits of the jezero crater paleolake system, mars. *Journal of*.

Hayes, A. G., Corlies, P., Tate, C., Barrington, M., Bell, J. F., Maki, J. N., ... Winchell, K. (2021, February). Pre-flight calibration of the mars 2020 rover mastcam zoom (Mastcam-Z) multispectral, stereoscopic imager. *Space Sci. Rev.*, *217*(2), 1–95.

Hayes, A. G., Grotzinger, J. P., Edgar, L. A., Squyres, S. W., Watters, W. A., & Sohl-Dickstein, J. (2011, April). Reconstruction of eolian bed forms and paleocurrents from cross-bedded strata at victoria crater, meridiani planum, mars. *J. Geophys. Res.*, *116*(E00F21).

Horgan, B., Udry, A., Rice, M., Alwmark, S., Amundsen, H. E. F., Bell, J. F., III, ... Wiens, R. C. (2023, July). Mineralogy, morphology, and emplacement history of the maaz formation on the jezero crater floor from orbital and rover observations. *J. Geophys. Res. Planets*.

Kinch, K. M., Madsen, M. B., Bell, J. F., Maki, J. N., Bailey, Z. J., Hayes, A. G., ... Sørensen, A. N. (2020). Radiometric calibration targets for the Mastcam-Z camera on the mars 2020 rover mission. *Space Sci. Rev.*, *216*, 1–51.

Le Mouélic, S., Enguehard, P., Schmitt, H. H., Caravaca, G., Seignovert, B., Mangold, N., ... Civet, F. (2020, June). Investigating lunar boulders at the apollo 17 landing site using photogrammetry and virtual reality. *Remote Sensing*, *12*(11), 1900.

Maki, J. N., Gruel, D., McKinney, C., Ravine, M. A., Morales, M., Lee, D., ... Algermissen, S. (2020, November). The mars 2020 engineering cameras and microphone on the perseverance rover: A Next-Generation imaging system for mars exploration. *Space Sci. Rev.*, *216*(8), 137.

Mangold, N., Gupta, S., Gasnault, O., Dromart, G., Tarnas, J. D., Sholes, S. F., ... Williford, K. H. (2021, November). Perseverance rover reveals an ancient delta-lake system and flood deposits at jezero crater, mars. *Science*, *374*(6568), 711–717.

Maurice, S., Wiens, R. C., Bernardi, P., Caïs, P., Robinson, S., Nelson, T., ... Wong, K. W. (2021, April). The SuperCam instrument suite on the mars 2020 rover: science objectives and mast-unit description. *Space Sci. Rev.*, *217*(3), 47.

Over, J.-S. R., Ritchie, A. C., Kranenburg, C. J., Brown, J. A., Buscombe, D. D., Noble, T., ... Wernette, P. A. (2021). *Processing coastal imagery with agisoft metashape professional edition, version 1.6—structure from motion workflow documentation* (No. 2021-1039). US Geological Survey.

Paar, G., Mett, M., Ortner, T., Kup, D., & Kontrus, H. (2022, June). High-resolution real-time multipurpose tunnel surface 3D rendering. *Geomech. Tunn.*, *15*(3), 290–297.

Paar, G., Ortner, T., Tate, C., Deen, R. G., Abercrombie, P., Vona, M., ... Barnes, R. (2023). Three-Dimensional data preparation and immersive Mission-Spanning visualization and analysis of mars 2020 Mastcam-Z stereo image sequences. *Life Support Biosph. Sci.*, *10*(3), e2022EA002532.

Prepared by the Mars Sample Return Campaign Science Group (MCSG), Czaja, A. D., Zorzano, M.-P., Kminek, G., Meyer, M. A., Beaty, D. W., ... Members (2023, June). Report of the science community workshop on the proposed first sample depot for the mars sample return campaign. *Meteorit. Planet. Sci.*, *58*(6), 885–896.

Quantin-Nataf, C., Alwmark, S., Calef, F. J., & others. (2023). The complex exhumation history of jezero crater floor unit and its implication for mars sample return. *Journal of*.

Quinn, D. P., & Ehlmann, B. L. (2019, August). A PCA-based framework for determining remotely sensed geological surface orientations and their statistical quality. *Earth Space Sci.*, *6*(8), 1378–1408.

Ruoff, N. A., Deen, R. G., Pariser, O. (2023). Mars 2020 camera software interface specification (SIS) [Computer software manual]. JPL Doc ID: D-99960, Jet Propulsion Laboratory.

Schon, S. C., Head, J. W., & Fassett, C. I. (2012, July). An overfilled lacustrine system and progradational delta in jezero crater, mars: Implications for noachian climate. *Planet. Space Sci.*, *67*(1), 28–45.

Stack, K. M., Williams, N. R., Calef, F., 3rd, Sun, V. Z., Williford, K. H., Farley, K. A., ... Yingst, R. A. (2020, December). Photogeologic map of the perseverance rover field site in jezero crater constructed by the mars 2020 science team. *Space Sci. Rev.*, *216*(8).

Traxler, C., Ortner, T., Hesina, G., Barnes, R., Gupta, S., Paar, G., ... Willner, K. (2022, April). *The PRoViDE framework: Accurate 3D geological models for virtual exploration of the martian surface from rover and orbital imagery.* Wiley.

Wiens, R. C., Maurice, S., Robinson, S. H., Nelson, A. E., Cais, P., Bernardi, P., ... Willis, P. (2021). The SuperCam instrument suite on the NASA mars 2020 rover: Body unit and combined system tests. *Space Sci. Rev.*, *217*(1), 4.

Supporting Information for "Stratigraphic reconstruction and analysis of the delta remnant Kodiak in Jezero Crater, Mars"

C. D. Tate[1], A. H. Hayes[1], O. A. Kanine[2], S. Gupta[3], G. Caravaca[4], G. Paar[5], S. Le Mouélic[6], C. Traxler[7], J. Rice[8]

[1]Cornell University, Department of Astronomy and Planetary Science, Ithaca, NY, USA
[2]California Institute of Technology Division of Geological and Planetary Sciences, Pasadena, CA, USA
[3]Imperial College London, Department of Earth Science and Engineering, London, UK
[4]Institut de Recherche en Astrophysique et Planétologie, CNRS, Université de Toulouse, CNES, France
[5]Joanneum Research, Institute for Digital Technology, Graz, Austria
[6]CNRS Délégation Bretagne et Pays de Loire, Nantes, France
[7]VRVis Zentrum für Virtual Reality und Visualisierung Forschungs-GmbH, Wien, Austria
[8]Arizona State University, School of Earth and Space Exploration, Tempe, AZ, USA

Contents of this file

Additional Supporting Information (Files uploaded separately)

1. OBJ wavefront model of Kodiak
2. PNG orthographic images of Kodiak described in S3
3. Excel spreadsheet, "tables.xlsx" with Tables 1, 2, S1, S2, and other information described in S4
4. PRo3D Annotation file described in S4

S1. Mars 2020 observations

Tables S1 and S2 list the Mars 2020 observations of Kodiak for the first 800 sols of the Mars 2020 mission. The Mastcam-Z observations (Table S1) are limited to images taken at its highest resolution zoom level at 110 mm. The Sol is the Martian day after landing, and the LMST is the local mean standard time. The sequence identification numbers are given for each. The azimuth and range values are measured from the rover's imaging location to the northeast edge of Kodiak. The resolution (Res.) is the pixel scale at Kodiak's distance (the product of the distance and Mastcam-Z 110mm ifov). The "used" column denotes whether the images were included in Kodiak's final reconstruction. The primary reason for not using a set of images is because they were taken at times of day with unfavorable lighting. Sols 418 and 548 imaged Kodiak when it was backlit and largely shadowed. This was more of an issue for the SuperCam RMI images since this solar geometry caused high levels of stray light in its optics and rendered the images unusable. Note that S1 does not include images taken at focal lengths other than 110mm. Our reconstruction used several 34 mm and 63 mm mosaics of Kodiak when their locations filled large gaps in the 110 mm dataset or helped make the control point network more robust. We similarly used Navcam images for the early stages of aligning widely spaced image stations.

S2. Reconstruction Range Error

Equation 1 gives the pixel scale s of an image taken from a distance d from its target. Pixel scale estimates the best possible resolution the camera can achieve without super-resolution. A camera's actual resolution, or the limit of its resolving power, is typically much larger than one pixel.

$$s = id. \tag{1}$$

Equation 2 gives the precision with which a pair of stereo images can estimate the range of a feature correspondent in both images. This equation comes from the Mars 2020 Camera Software Interface Specification (SIS) (?, ?), which describes the PDS-compliant image data products from all Mars 2020 cameras.

$$e = ic\frac{r^2}{b}, \tag{2}$$

where e is the range error, i is the camera's instantaneous field of view ($ifov = 67\ \mu rad$ for Mastcam-Z at 110mm focal length), c is the correlation accuracy in pixels (usually $c = 0.25$ pixels), r is the stereo range distance, and b is the effective baseline between the two imaging locations. This range error estimation is appropriate for stereo pairs taken under identical lighting conditions and at small angular separations, $b/r \ll 1$. Although this equation simplifies a complex problem, it must be enfranchised that eq 2 breaks down for large baseline distances relative to range. For instance, the maximum stereo disparity in this dataset is between azimuths, $az_{max} - az_{min} = 140°$, for which $b > r$ and eq. 2 would not give an appropriate estimate range error. Therefore, it is necessary to account for what happens to reconstruction errors for an arbitrary number of stereo pairs with pair-wise stereo disparities that do not follow the small angle approximation.

Estimating realistic range errors requires accounting for several second-order effects absent in eq. 2. Foremost, structure from motion (SfM) is a multi-stereo technique not strictly limited by individual stereo pairs (refs). Another effect not captured in eq. 2 is how the stereo correlation parameter c changes with increasing stereo disparity ratio b/r. Undoubtedly, the correlation becomes less precise as the projected features on the terrain surface diverge at wide angles. Part of this effect would be due to the breakdown in the small angle approximation. Still, the primary cause would be the inherent confusion in the tie point matching between the stereo pairs over terrain with complex topography. Although this becomes a scene-relevant source of error,

0094-8276/23/$5.00

we wish to identify a reasonable limit on the stereo disparity ratio. One such limit happens at a disparity angle of 14 degrees (or a disparity ratio of $b/r = 0.25$), beyond which eq. 2 could significantly underestimate the range error. Taking a maximum stereo disparity ratio of $(b/r)_{max} \approx 0.25 \approx c$, the minimum range error becomes the product of ifov and range, which simplifies to the approximate pixel scale,

$$e_{min} = ir. \tag{3}$$

Notably, this minimum range error approximately equals the pixel scale $e_{min}(r) \approx s(d)$ where $r \approx d$. Since it does not make physical sense for range error to be more precise than the lateral pixel scale, $e < s$, we justify $(b/r)_{max} \approx c$ as a reasonable limit on the meaningful extracting of topological information from stereo imaging. Therefore, we estimate the range error by evaluating eq. 2 at average adjacent disparity angles of the dataset taken from $N = 20$ imaging locations,

$$(b/r)_{eff} = tan\left(\frac{az_{max} - az_{min}}{N-1}\right) \approx 0.13, \tag{4}$$

which is 7° disparity angle. The effective disparity ratio can also be assumed to be half of the maximum value, $(b/r)_{eff} \approx \frac{1}{2}(b/r)_{max} \approx \frac{1}{2}c$. In either case, the effective maximum range error of this dataset is approximately twice the pixel scale,

$$e_{max} \approx 2id. \tag{5}$$

In the present case for a model made from a large number of imaging locations ($N \gg 2$) that are semi-uniformly distributed over an extensive range of azimuths ($az_{max} - az_{min} \gg 1$), the estimated range error is reasonably between the pixel scale and twice the pixel scale, $s < e \leq 2s$. For simplicity, therefore, we can assume that the range error of this SfM reconstruction is equivalent to the pixel scale.

S3. Orthographic maps and projections of Kodiak

The images in Fig. 3 are orthographic renderings of the model from four directions: up, north, east, and northeast. We uploaded full-resolution PNG images separately in the supplemental data. We include several other orthographic projections. These include a set of three images that show Kodiak's northern outcrops from approximately the Sol 580 location with the Mastcam-Z images (Fig. S4b), SuperCam images (Fig. S4c), and both (Fig. S4d) projected onto our model of Kodiak.

S4. PRo3D

We use PRo3D for our 3D analysis. Fig. S2 shows a sample of the layer traces used in this study. We present a complete record of our traces in several forms. The attached spreadsheet (”tables.xlsx”) has a tab named ”Table A3” that gives high-level information about each of the two dozen regions on Kodiak where we performed quantitative strike and dip analysis. This table shows the region name (arbitrarily assigned), type (e.g., topset, foreset, bottomset), medium dip angle, medium dip azimuth, number of measurements, and a PRo3D screenshot graphically showing its location on Kodiak. Another tab, ”Table A3 long version” gives the measurement and uncertainty values for every line trace. This includes each measurement strike (azimuth minus 90 degrees), dip angle, rake angle, and the max and min angular error estimated by the PCA-based plane-fitting algorithm (Quinn & Ehlmann (2019)). Additional columns give the trace's region name as defined in tab ”Table A3”; the dip color using the same color map as Fig. 3 (a); and the number of points we selected on the model to define the trace. We ordered the first six columns of tab ”Table A3 long version” for direct copy and paste into Daven Quinn's website, Uncertain orientations plotter `https://davenquinn.com/projects/attitude/plotter`. This tool specializes in graphically inspecting the error space of strike and dip measurements.

S5. Additional measurements on Kodiak and Whale Mountain

Whale Mt. is attached to the Western Jezero Delta and stands about 1 km west of Kodiak. There are several notable similarities and differences between these two geological features. It could be a coincidence that Whale Mt is the closest part of the delta to Kodiak. Figure S3 is similar to Figure 3 but lacks several annotations that may obscure some features of interest. Figure S4 shows our dip and strike measurements on Whale Mountain, which preserves a delta lobe-like feature similar in scale to the northeast ”nose” of Kodiak.

The primary similarity is Whale Mt's dome-shaped layers to the nose of Kodiak's Unit 1. The layers in Whale Mt dip between azimuths of 60 and 210 with a median value of about 120 N. This direction is nearly orthogonal to Kodiak's nose, which dips between 180 to 240 N with a median of about 200 N. Both features have consistently changing layers over scales of 50 m. This scale is small for a Gilbert-style delta foreset. However, this is less likely to be an anomaly because there are two examples in the delta front area.

Table S1. Mastcam-Z observations of Kodiak taken at its highest zoom lever at 110mm focal length. The images taken after Sol 580 are not used our 3D reconstruction.

Sol	LMST	Sequence	Azimuth [°N]	Range [m]	Res. [cm/pix]	Used	Notes
4	14:07	zcam00024	84.0	2298	16	no	-
57	10:48	zcam08103	84.0	2369	17	yes	-
63	8:29	zcam08022	84.0	2369	17	no	with Scam RMI
69	8:46	zcam03120	84.4	2376	17	no	-
77	7:32	zcam08036	85.0	2390	17	no	with Scam RMI
83	7:58	zcam03132	85.0	2390	17	yes	Scam RMI
94	12:14	zcam08054	85.3	2368	17	no	too late in day
104	12:30	zcam08065	86.4	2307	16	no	too late in day
105	15:26	zcam08071	87.8	2276	16	no	too late in day
108	11:46	zcam08075	88.0	2275	16	yes	only south side visible
111	10:43	zcam08084	90.5	2215	16	yes	-
114	12:08	zcam08092	91.4	2210	15	no	too late in day
121	11:38	zcam08114	92.2	2203	15	no	-
128	10:45	zcam08128	94.7	2240	16	yes	-
130	11:30	zcam08132	95.1	2267	16	no	-
135	10:46	zcam08138	101.2	2411	17	yes	-
149	11:49	zcam08160	104.6	2436	17	no	occluded
207	12:35	zcam08235	102.8	1856	13	no	occluded
214	10:54	zcam08251	102.2	1835	13	yes	occluded
248	8:27	zcam08270	101.6	1882	13	no	with Scam RMI
275	9:17	zcam08292	101.6	1882	13	yes	-
284	11:45	zcam08305	102.8	1837	13	no	Kodiak occluded
290	7:32	zcam08315	104.5	1809	13	no	Kodiak occluded
382	9:36	zcam08410	78.8	2528	18	yes	-
383	9:36	zcam08411	77.2	2809	20	yes	-
388	8:10	zcam08416	64.2	3212	22	yes	very long distance
409	10:10	zcam08425	18.8	784	5	yes	-
414	10:04	zcam08428	-3.4	701	5	yes	-
415	15:40	zcam08430	-24.0	527	4	yes	-
416	16:00	zcam08433	-28.9	478	3	yes	-
418	10:09	zcam08438	-28.9	478	3	no	with Scam RMI
470	12:49	zcam08491	-9.8	1050	7	yes	too late in day
548	13:00	zcam08565	-23.3	580	4	no	with Scam RMI, stray light
580	15:11	zcam08598	-36.3	701	5	yes	with Scam RMI
693	12:35	zcam08688	-3.8	717	5	no	after sol 580
711	11:28	zcam08714	-16.1	1255	9	no	after sol 580
753	16:03	zcam08758	-43.6	2397	17	no	after sol 580
756	15:43	zcam08765	-44.5	2514	18	no	after sol 580
762	11:46	zcam08774	-40.1	2521	18	no	after sol 580

Table S2. SupterCam RMI imaging sequences of Kodiak.

Sol	LMST	Sequence	Azimuth [°N]	Range [m]	Res. [cm/pix]	Images	Used	Notes
63	8:12	scam01063	84.0	2369	2.47	10	yes	-
77	8:25	scam02077	85.0	2390	2.50	2	yes	-
248	8:06	scam01248	101.6	1882	1.97	10	yes	-
418	8:57	scam01418	-28.9	478	0.50	10	no	stray light
548	12:40	scam04548	-23.3	580	0.61	4	no	stray light
548	12:50	scam05548	-23.3	580	0.61	4	no	stray light
580	15:17	scam01580	-36.3	701	0.73	12	yes	-

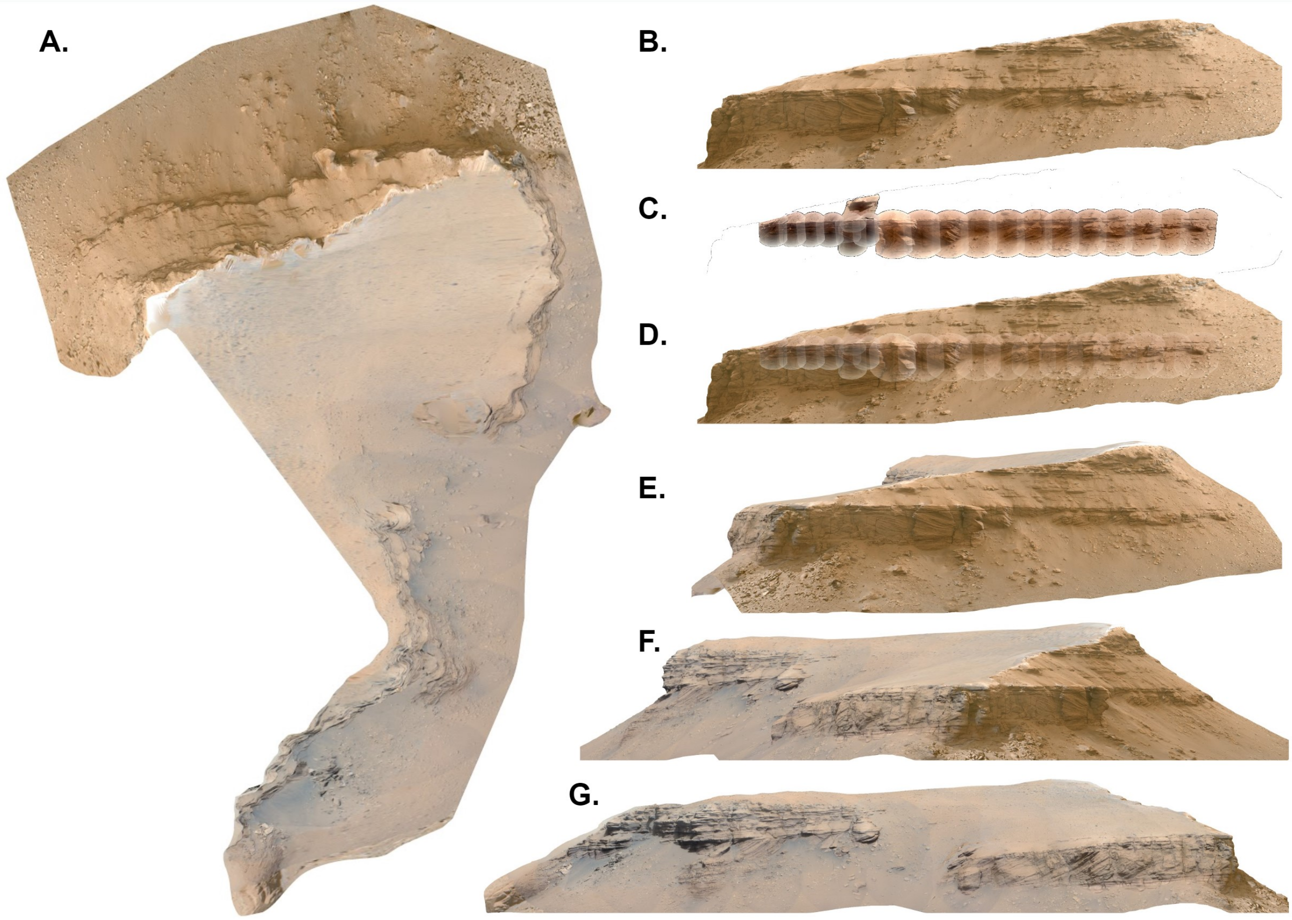

Figure S1. Rendered Orthographic Images of Kodiak. The full-scale images are downloadable from supplementary materials. Each image filename is in parentheses below. (a) plane view same as Fig. 3a (Kodiak_top.png); (b) Kodiak's northern outcrops from approximately the Sol 580 location (Kodiak_sol580_scam_only.png); (c) is the same as (b) but with only SuperCam RMI image projections (Kodiak_sol580_scam_only.png); (d) is the same as (b) and (c) with the Supercam RMI images projected on top of the Mastcam-Z images (Kodiak_sol580_scam_zcam.png); (e) northern view and same as Fig. 3b (Kodiak_north.png); (f) northeastern view and same as Fig. 3c (Kodiak_northeast.png); (g) eastern view and same as Fig. 3d (Kodiak_east.png)

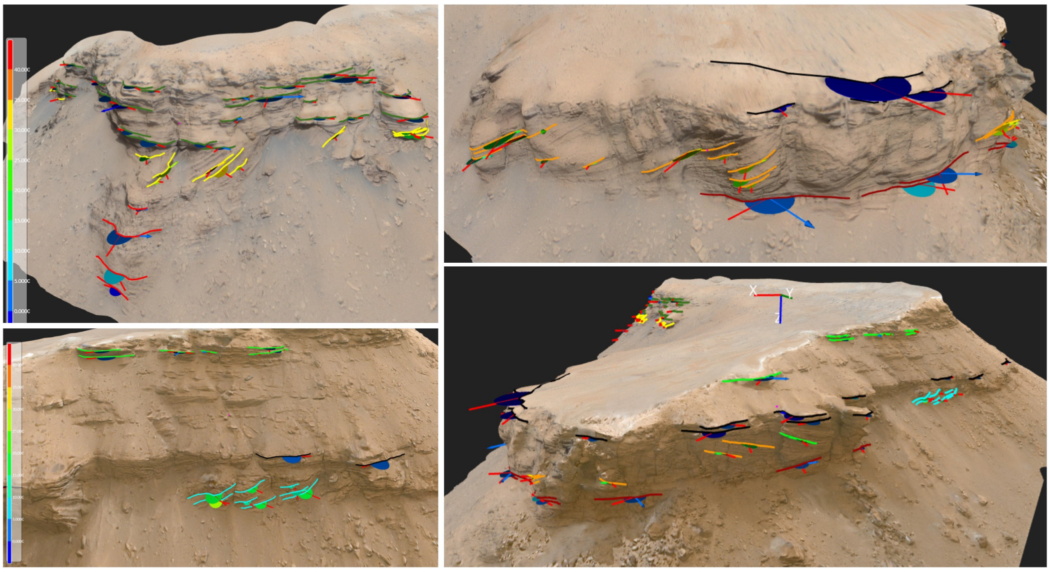

Figure S2. Views from the PRo3D software, in which we trace the best-exposed layers and solve for their geometric properties.

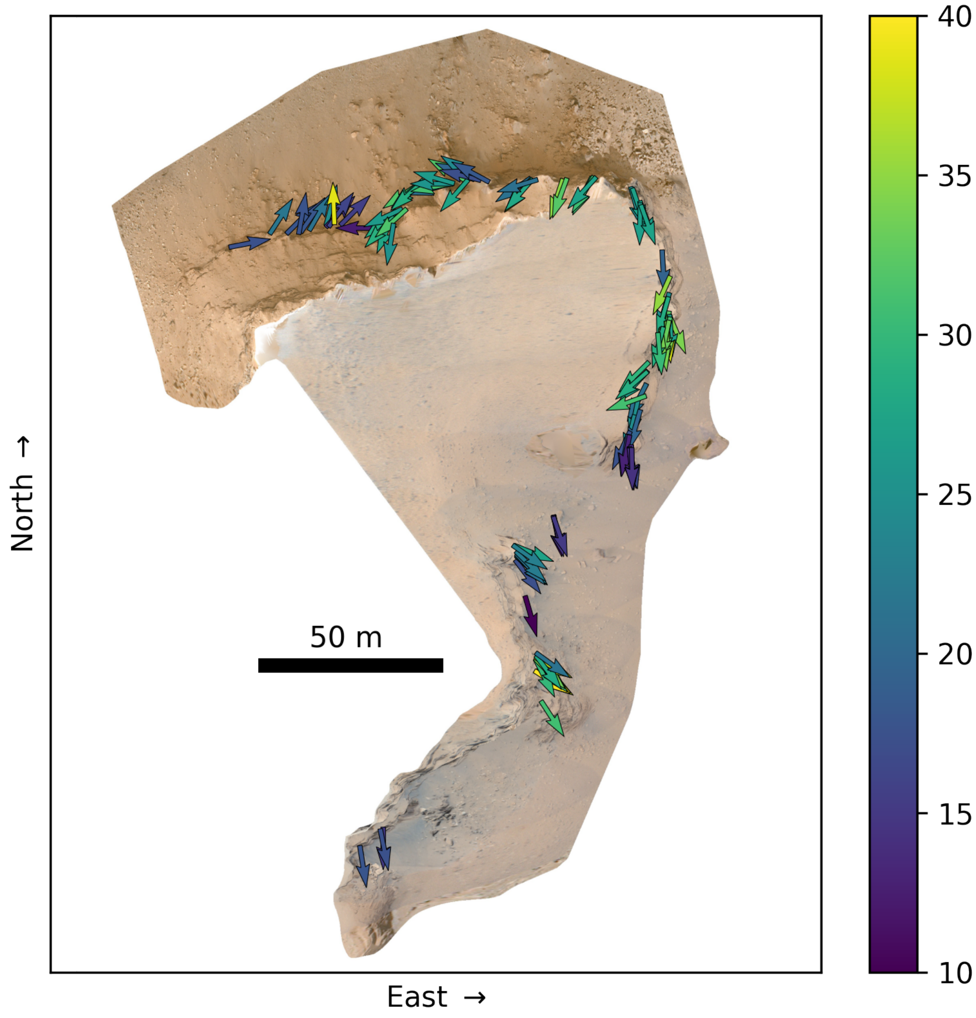

Figure S3. Orthgraphic projection Kodiak with strike and dip annotations. These data are identical to Fig. 3.

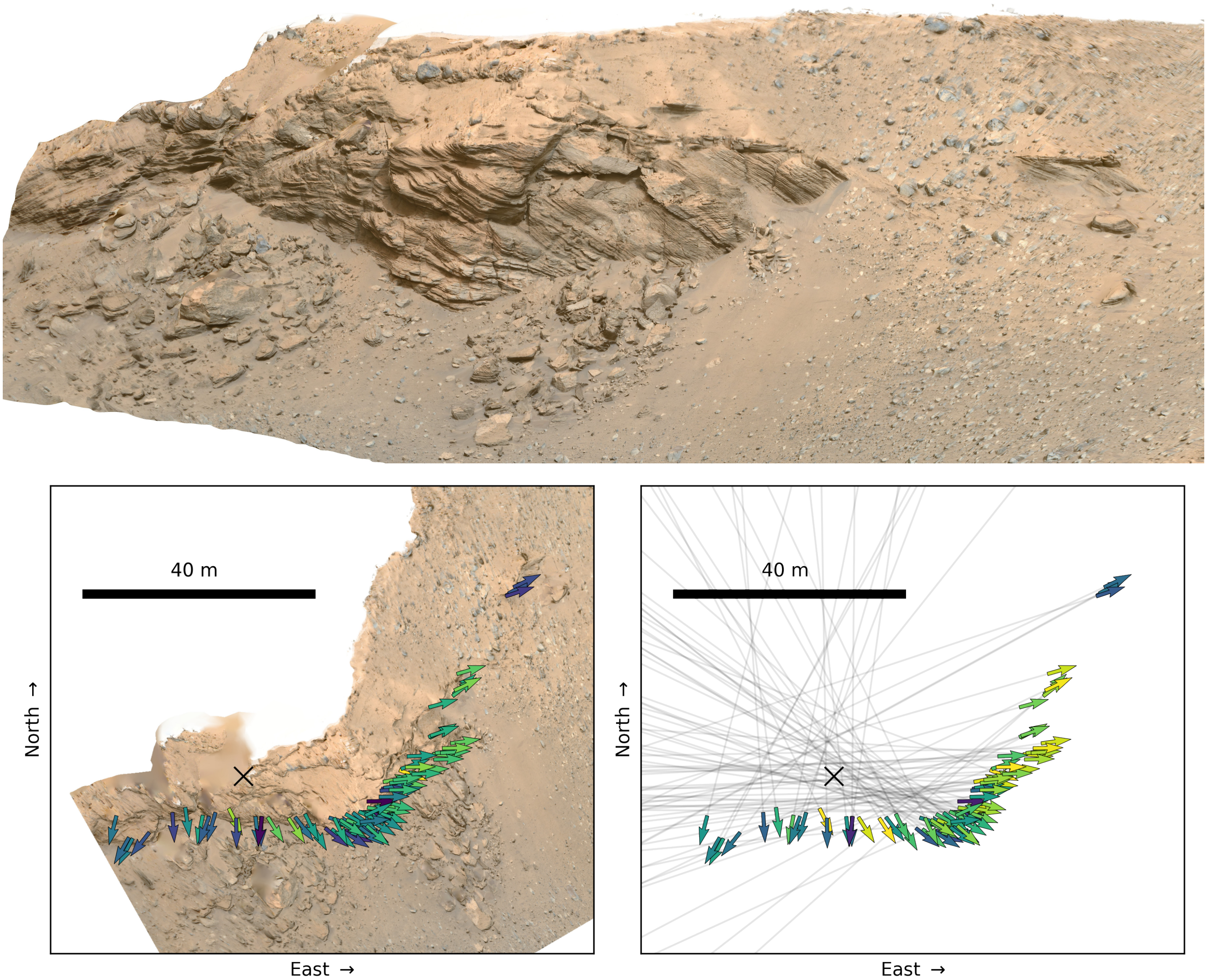

Figure S4. Orthgraphic projections of Whale Mountain and strike and dip annotations. The top image (a) is Whale Mountain from the Northeast direction. In this projection, up is up, and right is Northwest [add subplot letters, a North arrow, and a scalebar]. The bottom left (b) is a plane view orthographic projection with arrows showing the dip azimuths and color showing the dip angle. The bottom right (c) shows lines extending from. The dip colors use the same colorbar scale as Fig. S4.